Astronomy & Astrophysics manuscript no. output
February 4, 2019

The Solar Orbiter Heliospheric Imager (SoloHI)

R. A. Howard[1⋆], A. Vourlidas[2], R. C. Colaninno[1], C. M. Korendyke[1], S. P. Plunkett[1], M. T. Carter[1], D. Wang[1], N. Rich[1], S. Lynch[1], A. Thurn[1], D. G. Socker[1], A. F. Thernisien[1], D. Chua[1], M. G. Linton[1], S. Koss[1], S. Tun-Beltran[1], H. Dennison[1], G. S. Stenborg[1], D. R. McMullin[3], T. Hunt[3], R. Baugh[3], G. Clifford[4], D. Keller[5], J. R. Janesick[5], J. Tower[5], M. Grygon[5], R. Farkus[5], R. Hagood[6], K. Eisenhauer[6], A. Uhl[6], S. Yarulshami[6], L. Smith[6], P. C. Liewer[7], M. C. Velli[8], J. Linker[9], V. Bothmer[10], P.Rochus[11], J.-P. Halain[11], P. L. Lamy[12], F. Auchere[13], R. A. Harrison[14], S. Patsourakos[15], O. C. St. Cyr[16], H. Gilbert[16], H. Maldonado[16], C. Mariano[16], and J. Cerullo[17]

[1] Naval Research Laboratory, Washington, DC, 20375, USA
[2] Johns Hopkins University Applied Physics Laboratory, Laurel, MD, 20723, USA
[3] Space Systems Research Corporation, Alexandria, VA, 22314, USA
[4] Silver Engineering, Inc., Melbourne, FL, 32904, USA
[5] SRI International, Princeton, NJ, 08540, USA
[6] SGT Technologies, Greenbelt, MD 20770, USA
[7] Jet Propulsion Laboratory, Pasadena, CA 91011, USA
[8] University of California Los Angeles, Los Angeles, CA 90095, USA
[9] Predictive Sciences Inc., San Diego, CA, 92121, USA
[10] University of Gottingen, Gottingen, Germany
[11] Centre Spatiale de Liege, University of Liege, Liege, Belgium
[12] Laboratoire Atmosphères, Milieux, Observations Spatiales, Guyancourt, France
[13] Institut d'Astrophysique Spatiale, Orsay, France
[14] Rutherford Appleton Laboratory, Harwell Oxford United Kingdom
[15] University of Ioannina, Ioannina, Greece
[16] NASA Goddard Space Flight Center, Greenbelt, MD 22070, USA
[17] ASRC Federal Space and Defense, Beltsville, MD 20705. USA

Received February 4, 2019; accepted Mon DD, 2019

ABSTRACT

Aims. We present the design and pre-launch performance of the Solar Orbiter Heliospheric Imager (SoloHI) which is an instrument prepared for inclusion on the ESA/NASA Solar Orbiter mission, currently scheduled for launch in 2020.
Methods. The goal of this paper is to provide details of the SoloHI instrument concept, design and pre-flight performance to give a potential user of the data a better understanding of how the observations are collected and the sources that contribute to the signal.
Results. The paper discusses the science objectives, including the SoloHI-specific aspects, before presenting the design concepts, including the optics, mechanical, thermal, electrical, and ground processing. Finally, the list of planned data products is also presented.
Conclusions. The performance measurements of the various instrument parameters meet or exceed the requirements derived from the mission science objectives. SoloHI is poised to take its place as a vital contributor to the science success of the Solar Orbiter mission.

Key words. Sun:corona / Zodiacal Light / Space Vehicles:Instruments / Telescopes / Instrumentation:Miscellaneous

1. Introduction

1.1. Overview

The Solar Orbiter mission (Müller et al. 2013, 2019), currently scheduled to launch in February 2020, will study the inner heliosphere with a set of remote sensing instruments observing the Sun and solar corona and a set of *in-situ* instruments measuring the solar wind around the spacecraft. Together, the ten Solar Orbiter instruments will provide a complete description of the plasma making up the solar wind - its origin, transport and composition - vastly improving on the Helios (Schwenn & Marsch 1990) mission launched in 1974. Solar Orbiter reaches a minimum perihelion of 0.28 AU after a series of gravity assists from Venus and Earth, which will also raise the inclination of the orbital plane to at least 30° from the ecliptic plane (Garcia-Marirrodriga & et al. 2019). The Solar Orbiter minimum perihelion of 0.28 AU is very similar to the Helios perihelion of 0.3 AU, but combined with the out of the unique ecliptic viewing, Solar Orbiter will address a fundamental question of solar physics: How does the Sun create and control the heliosphere?

Solar Orbiter will combine *in-situ* measurements with high-resolution remote-sensing observations of the Sun in a systemic approach to resolve fundamental science problems needed to achieve this objective. These problems include the sources of the solar wind, the causes of eruptive releases of plasma and magnetic field from the Sun known as coronal mass ejections (CMEs), the evolution of CMEs and their interaction with the ambient solar wind flow, and the origins, acceleration mechanisms and transport of solar energetic particles that may be hazardous to both human explorers and robotic spacecraft that op-

⋆ Corresponding author: R. A. Howard e-mail: russ.howard@nrl.navy.mil

erate in the highly variable environment outside of Earth's magnetosphere.

The ten instruments on board the Solar Orbiter mission (Müller et al. 2019) include six remote sensing (RS) instruments observing the solar disk and corona, and four *in-situ* (IS) instruments measuring the plasma and magnetic field at the spacecraft. Two of the instruments, one IS and one RS, will observe the region between the Sun and spacecraft - the Radio and Plasma Wave instrument (RPW, Maksimovic et al. 2019) and the Solar Orbiter Heliospheric Imager (SoloHI). They will provide a link between the remote and local observations and enable the determination of the physical connectivity between the Sun and the solar wind. The RS telescope instruments have fixed optics which means that they observe a fixed angular field of view but the field, in terms of solar radii, varies as a function of heliocentric distance thanks to the elliptical orbit of the mission.

The combination of remote sensing instruments and *in-situ* instruments to study the Heliosphere is unique. The Ulysses mission (Wenzel et al. 1992; Marsden et al. 1986), launched in 1990, was in orbit about the Sun at high latitude and had a good complement of *in-situ* instruments but no remote sensing ones. The Helios spacecraft had one photometer that measured the Zodiacal Light (ZLP; Leinert et al. 1982) in addition to a complement of *in-situ* instruments. These excellent *in-situ* observations were often coupled with Earth-orbiting remote sensing instruments to link solar structures to *in-situ* ones (e.g. Sheeley et al. 1985) to great advantage.

The ZLP made excellent measurements of the light scattered by dust in the inner heliosphere, which is called the Zodiacal light (ZL) far from the Sun, and the F-corona close to the Sun. The ZLP found the ZL to be constant and symmetric. However, in a series of papers using the STEREO/HI instrument Stenborg and colleagues (Stenborg & Howard 2017b; Stenborg et al. 2018; Stauffer et al. 2018) found small deviations from constancy and symmetry.

The SoloHI is designed, built and operated by the U.S. Naval Research Laboratory. It will image the inner heliosphere over a wide field of view (FOV) by observing visible sunlight scattered by electrons in the solar wind and interplanetary dust. It builds on the success of the Heliospheric Imagers (Eyles et al. 2009) in the SECCHI suite (Howard et al. 2008) of telescopes on the STEREO mission (Kaiser et al. 2008), launched in 2006. The 40° circular FOV of SoloHI is centered on the orbital plane in latitude but it is offset from the Sun in longitude spanning elongations from 5.4° to 44.9° to the east of the Sun (i.e. in the anti-ram direction), as viewed by the Solar Orbiter spacecraft.

Scattering of photospheric light from dust will also contribute to the SoloHI signal. From 1 AU, this component is up to two orders of magnitude brighter than the electron-scattered component. However, we expect that the closer vantage point and the possibility of seeing dust sublimation (Sec. 2.5) will decrease the F-coronal signal. SoloHI will image the large-scale structure of the electron corona and allow observers to follow transient structures as they propagate in the inner heliosphere and ultimately pass over Solar Orbiter or other similar instrumentation such as the Parker Solar Probe (PSP; Fox et al. 2016)). The Wide Field Imager for Solar Probe (WISPR; Vourlidas et al. 2016) on the PSP has similar characteristics to the SoloHI. Together, SoloHI and WISPR will provide the crucial link between the remotely sensed and *in-situ* observations from Solar Orbiter, PSP and other inner heliospheric probes.

In the following sections we describe the SoloHI instrument. In Section 2 we present the Science Objectives, including the SoloHI unique objectives. In Section 3 we present an overview of the instrument. In Section 4, we describe the instrument design. In Section 5, we describe the operations concept, the data processing and the data products, and the ground system. Finally, we summarize in Section 6.

2. Science Objectives

The SoloHI science investigation has four science objectives that flow directly from the Solar Orbiter mission objectives (Müller et al. 2019) but are adapted to the SoloHI's measurement approach. Below are the objectives, in the form of questions, targeted by SoloHI. They are described in more detail in the rest of the section:

- What drives the solar wind and where does the coronal magnetic field originate?
- How do solar transients drive heliospheric variability?
- How do solar eruptions produce energetic particle radiation that fills the heliosphere?
- How does the solar dynamo work and drive connections between the Sun and the heliosphere?

The Solar Orbiter mission design is quite complex, involving perihelion and aphelion passages which do not always occur at the same heliocentric distance and/or with the same inclination relative to the ecliptic. For an imaging instrument such as SoloHI, these orbital variations imply both a changing field of view, in terms of heliospheric coverage, and varying spatial resolution, thus changing the optimum observing strategy and science focus for a given objective (e.g., shock formation versus turbulence studies). To appreciate the flexibility and performance of the proposed SoloHI instrument and to facilitate comparison with similar instruments at Earth orbit, we express the FOV and spatial resolution in terms of their 1 AU equivalent quantities using the symbol, AUeq, for shorthand.

To address the science objectives, a series of Science Activity Plans (SAPs) have been developed (Zouganelis et al. 2019). These plans define the instruments and their individual plans for addressing each of the SAPs. They are similar to the successful Joint Observing Programs developed for the SKYLAB and SOHO missions (Holt & da Silva 1977; Domingo et al. 1995). All the instruments have flexible capabilities that can be adjusted to explore this new region of space. To coordinate the modes and to help plan for the inputs to the SAPs, two working groups were formed, one for the RS instruments (Auchere et al. 2019) and another for the IS instruments (Horbury et al. 2019). Another input into the SAPs is coordination with the PSP (Velli et al. 2019), which has overlapping science objectives. The coordination of all of the inputs occurs within the Solar Orbiter Operations Working Group (SOWG; Zouganelis et al. 2019). One focus of the science planning activity is to identify what regions on the Sun might connect with the spacecraft. To assist in this effort, with the development of analysis tools and coordination with modeling, the Modeling and Data Analysis Working Group (MADAWG) was formed (Rouillard et al. 2019).

2.1. What Drives the Solar Wind and Where Does the Coronal Magnetic Field Originate?

White-light imaging with the Large Angle and Spectrographic Coronagraph (LASCO, Brueckner et al. 1995) and the Sun-Earth Connection Coronal and Heliospheric Investigation (SECCHI, Howard et al. 2008) coronagraphs have revealed a variety of

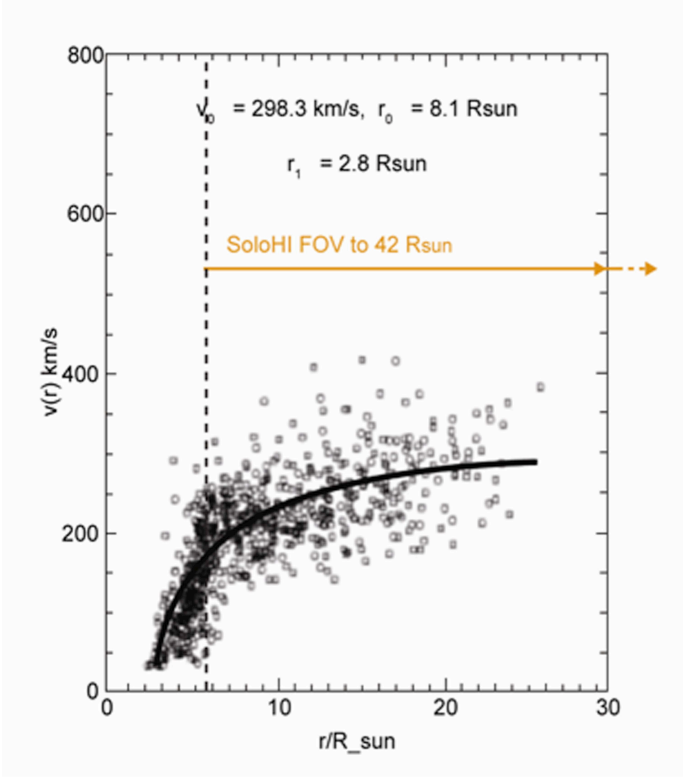

Fig. 1. Velocity measurements of streamer blobs with LASCO. The SoloHI FOV during perihelion passages is also shown. The solid line is a fit of the blobs to an exponential described in the text.

unexpected dynamical phenomena in the outer corona, including plasma blobs ejected continually from the cusps of streamers (Sheeley et al. 1997; DeForest et al. 2018), ray-like structures pervading the streamer belt (Thernisien & Howard 2006), swarms of small-scale inflows (e.g. Sheeley & Wang 2014) that occur during times of high solar activity, and coronal jets (Vibert et al. 2016), in which plasma and magnetic flux are exchanged between closed and open field regions of the corona. More recently, a direct association has been made between the outward flowing "blobs" and a corresponding inflow of "coronal rain" (Sanchez-Diaz et al. 2017), supporting the idea that "blobs" are the result of magnetic reconnection at the top of helmet streamers associated with the neutral line. Such reconnection processes have a bearing on questions as diverse as the formation and evolution of the heliospheric plasma/current sheet, the origin of the slow solar wind, the heliospheric magnetic flux budget, the solar-cycle evolution of the coronal field, and the rigid rotation of coronal holes.

While the reconnection sites will be observed with the Multi Element Telescope for Imaging and Spectroscopy (Metis; Antonucci et al. 2019) coronagraph and the Extreme Ultraviolet Imager (EUI; Rochus & et al. 2019) in the inner corona, SoloHI observations are essential for measuring the outer coronal and heliospheric signatures of these events. During perihelion, SoloHI will be able to trace the streamer blobs formed in the Metis FOV to much greater heights. The large uninterrupted FOV of SoloHI enables more accurate velocity and mass measurements, compared to LASCO or SECCHI, and the increased resolution and sensitivity of SoloHI will reduce the scatter in the outer velocity measurement shown in Figure 1. The three parameters at the top of the figure are the parameters in the fit shown as the solid line. The equation describing the flow speed is $V^2 = V_0^2$ [1 - $e^{-(R-R_1)/R_0}$]. *SoloHI will measure the velocity and acceleration profile of the transient slow solar wind flows and assess their role in the slow solar wind mass supply.*

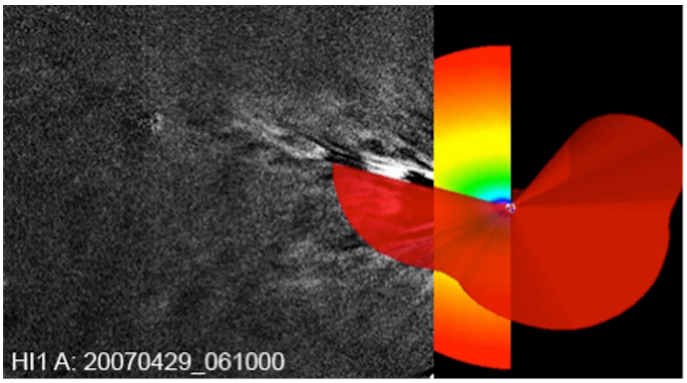

Fig. 2. Comparison of SECCHI/HI observation of solar wind structures (grey scale) with the model-derived location of the HCS (red surface). The meridional slice shows the model velocity which is not discussed here.

SoloHI will investigate the structures that comprise the heliospheric plasma sheet (HPS) and their solar origins, and the relation of the HPS to the heliospheric current sheet (HCS). For this, SoloHI will image the extension of streamer structures far into the heliosphere and compare their measured location and densities to *in-situ* measurements and models. Observations from the STEREO/HI telescopes have shown that this is possible. In Figure 2, taken from Vourlidas & Riley (2007), the location of the HCS, based on an MHD simulation, is projected onto a 2-hour SECCHI/HI running difference image showing quiescent solar wind structures. The figure shows that the largest intensity (therefore density) variability corresponds to locations nearest the HCS. In other words, SECCHI/HI can image the HPS directly and detect its intermittent structure. These measurements can identify the sources of the solar wind structures when compared with *in-situ* abundance measurements. SoloHI will have better sensitivity and spatial resolution than HI (see Table 1 in (Vourlidas et al. 2016) because it will fly closer, and in some cases, through the structures. This will allow us to trace the HPS boundaries, their evolution and their relation relative to the HCS in much greater detail than possible with STEREO. When combined with the *in-situ* observations from the Solar Orbiter, and/or PSP, the SoloHI observations will provide strong constraints on the origin and evolution of the solar wind plasma in the heliosphere.

Observations of the scattered light intensity also enable measurements of the solar wind density turbulence (e.g. Marsch 2000) directly from the SoloHI images. Because the observed emission is related to the number of electrons along the line of sight, intensity variations provide a direct measure of solar wind density variations, which can be compared to Earth-based interplanetary scintillation or PSP/Solar Orbiter *in-situ* measurements. SoloHI will run a specific observing program for this case (wave turbulence programs in Figure 21). For example, we can use the SoloHI Low Latency synoptic maps and MHD modeling to predict when PSP will cross a solar wind structure of interest (e.g., an HPS boundary or a fast stream interface). For a specific time interval, say 4 hours before the PSP passage, SoloHI will obtain images over a restricted FOV (about 1.5°x5°) around the region of interest. A 2D power spectrum of the density fluctuations can then be constructed from the imaging time series.

Such a program is made possible by the programming flexibility offered by the SoloHI electronics (see Section 5).

2.2. How Do Solar Transients Drive Heliospheric Variability?

To understand the propagation and evolution of CMEs into the heliosphere, we have until recently relied on MHD models to fill in the gap between the imaging observations restricted to small elongations from the Sun and *in-situ* measurements of interplanetary CMEs (ICMEs) at 1 AU. The gap has been filled, since 2007, with the observations from the heliospheric imagers onboard STEREO. The SECCHI/HIs have imaged and tracked a variety of density structures ranging from ICMEs (Rouillard et al. 2009a) to stream interaction regions (SIRs; Sheeley et al. 2008) to small flux ropes entrained in the SIRs (Rouillard et al. 2009b). We have found that CMEs rotate, deflect, distort (Liewer et al. 2015; Isavnin et al. 2014; Nieves-Chinchilla et al. 2012), and interact with each other (e.g. Shen et al. 2013) in the inner heliosphere.

Somewhat surprisingly, the uninterrupted corona-to-heliosphere imaging from SECCHI has not brought closure to many questions. The most glaring is the lack of agreement between *in-situ* and imaging-based reconstructions of CMEs (e.g. Wood et al. 2017). The speed profile, particularly of medium speed (<900 km/s) ICMEs, is difficult to establish (Colaninno et al. 2013). CME deformation may be nothing more than projection effects (Nieves-Chinchilla et al. 2012). These problems arise partially from the difference in the spatial scales detected *in-situ* and in the HIs and partially from the difference in the location of the measurements. Many events are difficult to track beyond the middle of the HI-1 FOV, above about 50-60 $R_\odot$, for example. The long exposure times (20 – 60 mins) and the use of running difference schemes to increase contrast obscure the fine structure within the ICMEs making it harder to associate *in-situ* and imaging features. Solar Orbiter and PSP offer an opportunity to solve some of these problems. SoloHI will extend the field of view of the SECCHI HI-1 to elongations greater than 40° from the Sun with increased sensitivity. It will also observe CMEs much closer to the sun, as they go over PSP (and Solar Orbiter) thus reducing the uncertainty, due to evolution, between remote sensing and *in-situ* analyses. *WISPR and SoloHI may observe the same CME from two very different vantage points for the first time.*

2.3. How Do Solar Eruptions Produce Energetic Particle Radiation that Fills the Heliosphere?

CME-driven shocks play a central role in determining the energetic particle populations in the heliosphere and in driving geospace storms. They are known to accelerate solar energetic particles (SEPs) to high energies (e.g., Reames 1999; Kahler 2001), even GeV energies (Bieber et al. 2004) during the so-called gradual SEP events. The geometry of the shock seems to play a further role in the observed variability of the spectral characteristics and composition of SEPs (Tylka et al. 2005). Many of these shock-related parameters (geometry, compression ratio, speed) are available or can be deduced from *in-situ* measurements at 1 AU. Recent SECCHI results (Kwon & Vourlidas 2018) demonstrate that some of these can finally be measured remotely in the low corona where the highest energy particles originate (≤2 $R_\odot$). The large scatter in the correlation between CME speeds and SEP peak intensities suggests a complex interplay among the CME speed, the acceleration mechanism(s) and the ambient environment. Much work has focused on the role of the variations of the environment through which the CME shocks and particles propagate (Gopalswamy et al. 2004; Kahler & Vourlidas 2005). Therefore, the height of formation of the shock, the 3-dimensional extent of the CME, and the existence or not of a preceding event are necessary observations for a better understanding of the generation and propagation of SEPs. SoloHI can provide these crucial observations, because it can image CMEs and their associated shocks at the coronal heights where the particles originate (≤10 $R_\odot$) with sufficient spatial resolution to resolve the locations of the CME-driven shocks.

The optimal period for such observations is during perihelion passages. For example, at the minimum perihelion, the SoloHI FOV, for the standard observation mode, extends from 5.2 to 42 $R_\odot$ with 52 arcsec resolution (AUeq) for 2x2 binned images. In other words, SoloHI is similar to a LASCO/C3 coronagraph with 2x better spatial resolution. SoloHI will readily observe and characterize the evolution of shocks. For example, a cadence of 30 min will allow 6 observations of a 2000 km/s CME in the SoloHI FOV during perihelion. The SoloHI inner FOV extends below 10 $R_\odot$ for all heliocentric distances within 0.5 AU, and therefore contributes to the SEP analysis for a much larger part of the Solar Orbiter orbit than just at perihelion. For these parts of the orbit, SoloHI will be able to observe shocks and CMEs as they go over PSP or other heliospheric probes.

To address the spatial extent of the shocks, the SoloHI observations can be combined with simultaneous observations from the SECCHI coronagraphs and imagers, WISPR, LASCO, or other near-Earth assets. The multipoint observations will be used to reconstruct the 3-dimensional structure of the CMEs and their associated shocks as shown in Kwon & Vourlidas (2018).

2.4. What is the Three-Dimensional Structure of the Heliosphere?

Our knowledge of the spatial extent and configuration of CMEs has been greatly improved thanks to 3D reconstructions afforded by the multi-viewpoint imaging from the SECCHI instruments (e.g. Thernisien & Howard 2006; Thernisien et al. 2009, 2011). LASCO provided a third viewpoint to SECCHI's. But there is a catch. All three lines of sight lay very close to the ecliptic plane providing partially redundant information. Having lost contact with STEREO-B on 1 October 2014, 3D reconstructions currently rely on the aging LASCO telescopes for the second viewpoint. Newmark et al. (2004) have shown that the resulting 3D reconstructions have large longitudinal uncertainties, which can be improved only with the addition of a viewpoint away from the ecliptic plane. These problems are exacerbated for 3D streamer reconstructions because their longitudinal boundaries are more difficult to define than CMEs. However, streamers are long-lived coronal structures, lasting for several rotations. We can rely on the solar rotation to provide additional viewpoints as shown by Frazin & Kamalabadi (2005). A temporal resolution of about 4.7 days (1/6 of the solar rotation) can be achieved with data from 3 satellites. Naturally, the rotational tomography approach is best suited for coronal reconstructions during periods of minimum activity although new techniques, such as Kalman filtering, seem to be able to capture some of the short-term evolution of coronal structures (Butala et al. 2005).

SoloHI will provide completely new information and constraints for understanding the 3D structure of the corona and CMEs. It will observe the heliosphere from out-of-ecliptic viewpoints, at varying latitudes and heliocentric distances, thus providing strong constraints on the longitudinal extent of the struc-

tures. The Solar Orbiter-Sun distance plays an important role in the data analysis because it affects the visibility of the Thomson scattered features in the images (see 2.5.2). In essence, the varying distance acts as a filter emphasizing structures that are progressively nearer the Thomson Surface (Vourlidas & Howard 2006) as it approaches the Sun. When combined with simultaneous white light observations from another viewpoint (e.g., LASCO, STEREO and/or PSP), the combined analysis should provide very strong constraints on the size of coronal features. The Solar Orbiter mission possesses another important advantage; within two weeks the spacecraft sweeps between its two latitudinal extremes (i.e. southern and northern extremes) thus enabling tomographic reconstructions of streamers using the SoloHI data alone with the same temporal resolution achievable currently by the LASCO instrument.

SoloHI will be the first instrument to provide high resolution imaging observations of Thomson-scattered emission from out of the ecliptic. SoloHI will be able to observe the interaction of the propagating CMEs with the solar wind and other CMEs from a unique vantage point. Depending on the inclination of the solar dipole during the high-latitude passes, SoloHI will be able to make a direct measurement of the longitudinal extension of the CME, the interaction of the CME with the boundaries of coronal holes and the interaction between CMEs, through a shorter line of sight than is possible from the ecliptic. The shorter line of sight will minimize uncertainties in these measurements due to the effect of overlapping structures. The question of how the solar wind variations are linked to the Sun at all latitudes encompasses the same detailed issues addressed in 2.2, but from different, out-of-the-ecliptic viewpoints. The connection between the *in-situ* solar wind and its solar sources will be analyzed with Solar Orbiter's measurements of solar wind speed, energy flux, magnetic field, chemical composition, and ionization state as functions of latitude. To get the full benefit of the out-of-ecliptic viewpoint in understanding the structure and dynamics of the corona, the SoloHI observations must be combined with the Metis, EUI, and SPICE (SpiceConsortium & et al. 2019) observations. Using the coronal imagers, we can observe the initiation and evolution of CMEs and more easily determine the spatial relation between CMEs and their coronal sources. At or near perihelion, when the SoloHI FOV enters the low corona, the combination with Metis and EUI will allow us to observe polar plumes and small-scale structures in the polar and equatorial coronal hole regions. *SoloHI provides the connecting link between the in-situ and solar surface measurements from Solar Orbiter in the inner heliosphere and the inner corona.*

2.5. SoloHI Unique Science

The visible emission at heights above 5 $R_\odot$ is dominated by scattering from interplanetary dust, the F-corona. It is a nuisance for coronal studies as it obscures the signal from CMEs and coronal streamers. Accurate removal of the F-corona is essential for the derivation of coronal density structure (e.g. Hayes et al. 2001), but the current F-coronal models are insufficient, as LASCO-C3 and SECCHI/HI-1 observations have shown. Stenborg & Howard (2017b) and Stenborg et al. (2018) found that the shape and intensity vary significantly as functions of ecliptic longitude and heliocentric distance and that the dust cloud is not a simple axisymmetric structure.

A different approach is required for the continuously varying scene in the SoloHI images. In preparation for the mission, a new technique to determine the background has been demonstrated successfully on the SECCHI/HI images (Stenborg & Howard 2017a). It uses a single image to generate a background model, under the assumption that the F-corona varies monotonically and smoothly.

In addition to the in-ecliptic views, which were well observed by SECCHI/HI and Helios (Leinert et al. 1981, 1998), Solar Orbiter's orbit will become inclined by at least 30° enabling us to extract quantitative measurements of the F-corona from a different viewpoint, yielding a more complete definition of the 3D distribution of dust in the inner heliosphere, and perhaps a short-term, time-dependent variation. We do not know, for example, whether comets are an important source of dust in the inner heliosphere. The detection of a significant population of large particles at high ecliptic latitudes would support this idea (Delsemme 1976). The combination of the SoloHI remote-sensing F-corona observations with dust models may allow the estimation of the size distribution of the dust in the inner heliosphere. In particular, the analysis of the changes in the distribution of particles below a few micrometers will yield information about the effects of solar radiation and plasma environment on the interplanetary dust (Mann et al. 2000; Jones et al. 2018).

A dust ring has been found around Venus (Leinert & Moster 2007; Jones et al. 2013, 2017), similar to the rings around many solar system objects. Do such rings exist around or in the neighborhood of Mercury? Finally, the SoloHI F-corona observations during the maximum of cycle 25 from high latitudes and within 0.5 AU provide an unprecedented, and probably unique, possibility to investigate whether CMEs interact in any significant way with the interplanetary dust and whether we can use this interaction to probe the CME magnetic fields, as suggested by Ragot & Kahler (2003), who predicted that the strong transient magnetic field in a CME can produce a temporary displacement of a small region of dust particles.

2.5.1. Signal to Noise

The total diffuse sky brightness observed by SoloHI is the sum of contributions from the F-corona (scattering from dust) and K-corona (scattering from electrons in the solar wind and CMEs), as well as integrated starlight from unresolved stars. The dominant contribution throughout the SoloHI FOV comes from the F-corona. In addition, numerous bright stars will be resolved as individual point sources of light. These stars will be removed from the images using techniques that have been developed and successfully implemented on SECCHI/HI.

The fundamental observational requirement is to obtain images with sufficient photometric precision to discriminate the K-corona, and its fluctuations (e.g., CMEs), from the other contributions to the total signal. Figure 3 shows a comparison of the 1-σ detection limit for the SoloHI with the expected signals. The detection limit shown here is for a single pixel and an exposure of 30 minutes at aphelion and 30 seconds at perihelion. The expected contribution of the F-corona was determined from the model of Koutchmy & Lamy (1985). The integrated starlight varies considerably with galactic latitude and longitude; an average contribution over the SoloHI FOV is shown in Figure 3. The expected contribution from CMEs is from Helios measurements by Jackson et al. (1985) and from SECCHI/HI measurements. The 1-σ detection limit remains below the expected CME signal over the full FOV. A signal-to-noise ratio (SNR) of 5 per spatial resolution element is required for threshold detection of a simple, known a-priori target on a flat background (Rose 1948; Barrett 1990), and substantially higher photon statistics (SNR>30) are required for more complex or unknown targets.

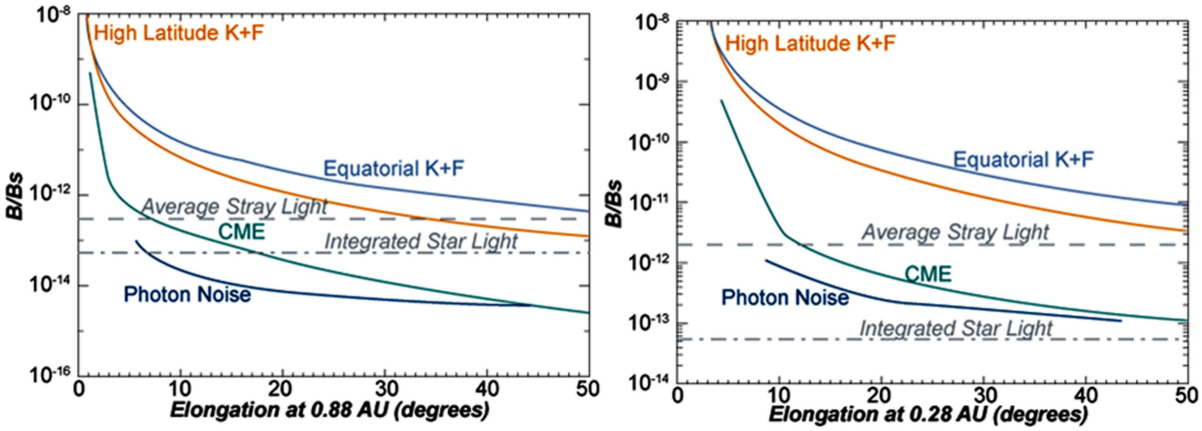

Fig. 3. Expected contributions to the SoloHI signal as a function of elongation angle for perihelion (0.28 AU) and aphelion (0.88 AU). The 1-σ photon noise detection limit per pixel is shown for an exposure of 30 min at aphelion and 30 sec at perihelion.

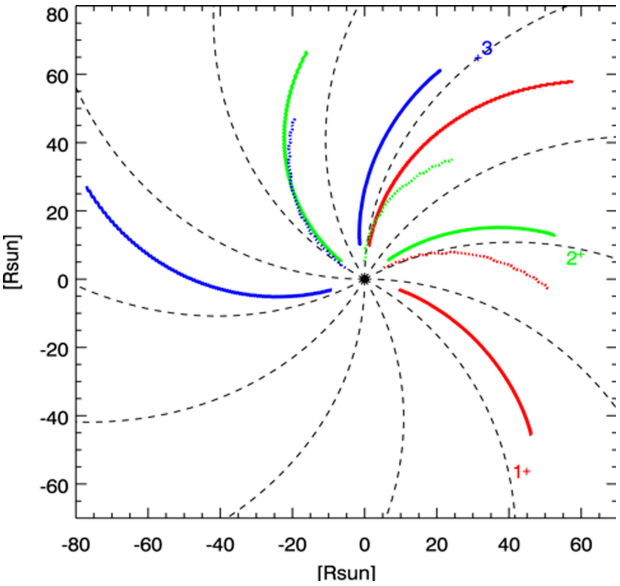

Fig. 4. Sensitivity map of the Thomson scattering emission for the Solar Orbiter-Sun geometries at perihelion. Each number denotes a location in the orbit ('2' is perihelion of 0.28 AU, while '1' and '3' are both at 0.34 AU). The 3 arcs in each color mark the locus of the 5%, 50%, and 95% brightness integrals along the line of sight. The extents of the arcs mark the SoloHI FOV. The dotted lines show the direction of the Parker Spiral for a 300 km/s wind.

These criteria are easily met over most of the SoloHI FOV. Near the outer part of the field, binning of pixels and/or longer integration times will be used to enhance the desired signal. At perihelion and/or in the inner part of the field, substantially higher cadence using subframes can be achieved without any degradation in resolution.

2.5.2. Thomson Surface Considerations

Solar wind features at progressively large angular distances from the Thomson surface scatter less than features close to the surface. Therefore, the SoloHI measurement sensitivity and its scene coverage are defined by the Thomson surface that varies with the Sun-observer distance (Vourlidas & Howard 2006).

Figure 4 shows an estimate of the SoloHI scene coverage for 3 SoloHI orbital positions along the orbit for the minimum perihelion, indicated by a number and a color . There are 3 curves for each SoloHI location that are plotted with the same color and define the distance along the SoloHI line-of-sight, where the integrated scene brightness reaches 5%, 50%, and 95% of its total brightness integral. 90% of the scene brightness captured by the SoloHI instrument lies between the 2 outermost solid-line curves. The numbers in Figure 4 refer to separate locations along the orbit. '2' is at the orbit perihelion of 0.28 AU, while '1' and '3' are both at 0.34 AU, on the inbound and outbound parts of the orbit. Any arc is indicating the location in the FOV, with the outer point on the arc being the largest elongation in the FOV and the inner point being the smallest elongation. The orbital transit time from position '1' to position '3' is approximately 17.6 days. As the SoloHI orbital position approaches its perihelion (position '2'), the SoloHI instrument primarily measures Thomson-scattered light from within 40 $R_\odot$ of Sun center and therefore becomes a local imager. This behavior of the scattering is very different than that at 1 AU.

The PSP orbits have perihelia from 35 $R\odot$ to 9. 8 $R\odot$. Because both PSP and Solar Orbiter are encounter missions, there is a small but finite probability that PSP will be in the field of view of SoloHI. When it is, Figure 4 demonstrates that SoloHI will easily detect the features passing over PSP while being sensitive to the solar wind flowing towards Solar Orbiter. This will provide an absolutely unique opportunity for joint observations.

3. Instrument Overview

SoloHI will perform remote observations of the Thomson-scattered white-light from the solar wind plasma of the inner corona with unprecedented resolution and cadence. SoloHI is a single, white light telescope of 20° half angle with the inner limit of the FOV at an elongation of 5° from Sun center. The objective lens has a 40° FOV and images the solar wind onto a matrix of four CMOS Advanced Pixel Sensor (APS) detectors with an effective total area of 3920x3920 pixels.

As the Solar Orbiter approaches the Sun, the spatial resolution will increase relative to the resolution at 1 AU and the absolute FOV correspondingly will decrease relative to 1 AU. At perihelion the SoloHI will have the same effective resolution as the SOHO LASCO/C2 coronagraph with a larger FOV (6-60 $R_\odot$) than the LASCO/C3 coronagraph and a higher signal-to-noise ratio than C3.

The key design aspects of SoloHI are to reject light from the solar disk to see the faint coronal signal with a good signal-

Table 1. SoloHI Instrument Parameters

Parameter	Value (M)easured (C)alculated
SIM Mass	15.18 kg (M)
SPS Mass	1.38 kg (M)
Volume	66.0 X_{SIM} x 40.5 Z_{SIM} x 29.1 Y_{SIM} (M) (Door Closed) x 50.8 Y_{SIM} (M) (Door Open)
Power	13.5 (w) (average)
Telemetry	53.2 Gbits/Orbit
FOV	40°x40° square limited to 48° at the detector corners
Image Array	3890 x 3890 Pixels (M); Note: Left 10 columns and bottom 10 rows of each die are opaque
Boresight Direction	Nominal: 25° from Sun center Measured: 25° 7'26.3"
Angular Range	5° - 45° from Sun center 5.25 $R_\odot$ - 47.25 $R_\odot$ at 0.28 AU
Angular Resolution	36.7 arc sec (Full) 73.5 arc sec (2x2 bin); 10.3 arc sec (Full) 20.6 arc sec (2x2 bin) equivalent at 0.28 AU
Spectral Bandpass	500 - 850 nm (M)
Exposure Time Per Image	Nominal 30 sec (C); Range 0.1-65 sec (M)
Number of Summed Images	Varies from 1-30 (C) depending on observing program, heliocentric distance and whether it is the inner or outer pair of die

to-noise ratio. The SoloHI baffles are designed to minimize the stray light entering the entrance aperture from various sources. For the Solar Orbiter mission there is a significant complexity - the solar light reflected by the solar array at the rear of the spacecraft onto the backs of the instrument baffles.

Table 1 gives a summary of the key instrument parameters. The parameters are either measured or computed and are indicated with an (M) or (C). The exposure time and number of summed images are calculated from our best estimates and could change in flight.

SoloHI is comprised of the SoloHI Instrument Module (SIM) and the SoloHI Power System box (SPS). The SoloHI functional block diagram (Figure 5) shows the components of the SIM and SPS. An interconnect harness (not shown) connects the SIM and the SPS and a spacecraft harness (not shown) connects SoloHI to the spacecraft.

Both SoloHI instrument units, the SIM and the SPS, are mounted on the exterior of the Solar Orbiter +Y panel. The SPS is located below the SIM and between the forward and aft SIM brackets that support the SIM. Figure 6 (top) shows the orientation of SoloHI with respect to the Solar Orbiter. The origin of the SIM Physical Reference Frame is located at the center of the aft SIM rigid instrument mount projected down to the base of the aft SIM bracket at the SIM mounting interface plane with the spacecraft deck. The XSIM axis points toward the Sun in its nominal orientation for science observations.

The SIM (Figure 6, bottom) includes the structure, the baffle assemblies (forward, interior and peripheral), the telescope, the SoloHI camera electronics (SCE), the baffle cover door assembly, the SIM thermal components, and the forward and aft SIM brackets. The SoloHI telescope is composed of the aperture hood assembly, the lens barrel assembly, and the focal plane assembly (FPA) and SCE. The SCE is composed of the processor card (PC), the camera electronics card (CC), and the SCE enclosure. The instrument telescope design is monolithic with no moving parts. The SPS includes the Relay Electronics Card (REC), the Power Electronics Card (PEC), the SPS enclosure, the SPS thermal components. Solar Orbiter provides operational power to the SPS and survival power to the SoloHI survival heaters on the SIM and SPS. In addition, Solar Orbiter forwards instrument commands and receives science data and housekeeping telemetry over the SpaceWire interface. Each pixel of the APS detector converts the photoelectric charge to volts, which is digitized off-chip, and the signal transferred to the SCE. The pixel is read out at the rate of 2 Mpixels/sec, The image data is processed and then sent to the spacecraft for storage on the solid state mass memory (SSMM) for later transmission to the ground. The APS is cooled passively by a radiator mounted to the side of the SIM with a view to deep space.

3.1. Design Philosophy

SoloHI meets the Solar Orbiter mission science objectives and instrument science objectives described in Section 2 with a design concept based on the heritage SECCHI/HI design tailored for the Solar Orbiter mission (Müller et al. 2019; Garcia-Marirrodriga & et al. 2019). The changes to the heritage design were made to conserve resources (mass, power, volume, and telemetry) to fit in the Solar Orbiter mission constraints. The Solar Orbiter mission orbital profile necessitates a small and relativity lightweight spacecraft. The mass, power, volume and telemetry requirements that we achieved are considerably smaller than the initial strawman baseline.

The two significant changes from the heritage SECCHI/HI are the larger single FOV and detector type. SoloHI has a single FOV that is double the size of the SECCHI HI1 inner telescope. By doubling the FOV, we can meet the science objectives with a single telescope. This change resulted in a significant savings in mass and volume. The second change was to use a custom complementary metal–oxide–semiconductor (CMOS) APS instead of the Charge-Coupled Device (CCD) that was used with SECCHI. The requirements for the SoloHI camera electronics are significantly reduced due to the increased functionality of the APS architecture on the chip, thereby reducing the mass and power compared to the CCD. The APS detector is described in more detail in Section 4.6.

3.2. Accommodation Challenges

Stray Light Two spacecraft components are in the optical field of regard (FOR) and particular attention was paid to them in the placement and surface treatments to reduce the stray light entering the entrance aperture to acceptable levels. One of the antennas from the Radio and Plasma Waves (RPW; Maksimovic et al. 2019) experiment passes through the FOR and could be easily accounted for, since it was located in the sunward direction. The more serious intrusion was from one of the 8.2m long panels of the solar array. Being at the rear of the spacecraft, reflections from the array and the mounting yoke heat shield reflect sunlight onto the backs of the linear forward occulters that block the direct radiation from the Sun. Reflected light hitting the backs of the linear occulters have access to the optical system. The mitigation techniques used to reduce the impact to acceptable levels are described in Section 4.3.

Dust Impacts Since the accommodation of the SoloHI package

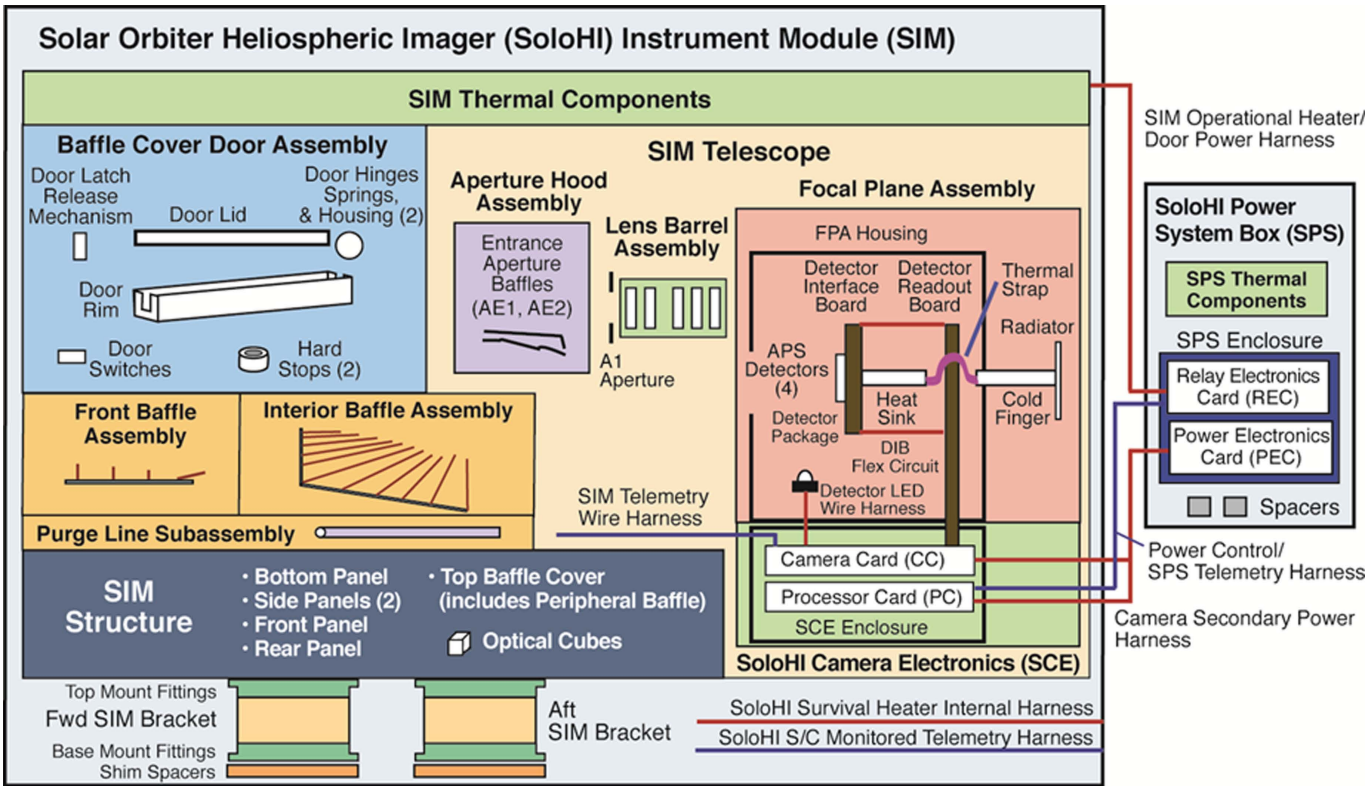

Fig. 5. SoloHI Functional Block Diagram

is on the anti-ram side of the spacecraft, and the optical field-of-view (FOV) is centered at 25° to the East of the solar vector, the likelihood of dust impacts was determined to be insignificant. The field of view is similar to the SECCHI/HI-1 telescope, which has had no detectable damage after 12+ years of operations, albeit at 1 AU.

Radiation Effects We used Solar Orbiter radiation guidelines for a seven-year mission for EEE parts selection. Our designs address single event effect (SEE) induced failure (latchup, burnout, gate rupture, secondary breakdown), non-destructive SEE (e.g., non-destructive latchup, mini-latchup, and single event functional interrupts) and single event-induced soft errors (including single event upsets (SEU) or transients in linear devices) and SEE-induced soft errors. All EEE parts meet the total ionizing dose (TID) requirement with a minimum radiation design margin of 2x the mission TID (60 kRad behind 2,54 mm of Al shielding). We used no EEE parts having a linear energy transfer (LET) threshold of <25 MeV cm^2/mg (SEU) or 100 MeV cm^2/mg. The selected APS detector technology (see Section 3.4) mitigates potential problems of Non-Ionizing Energy Loss (NIEL) and radiation-induced Charge Transfer Efficiency (CTE) losses. Unlike CCDs (e.g. LASCO, SECCHI/HI), the photoelectrons are read-out from each APS pixel without shifting through the rest of the detector, and therefore have a reduced (but not negligible) susceptibility to radiation-induced loss in CTE. Like CCDs, the radiation-induced damage increases the dark current, dark current non-uniformity noise, particle-induced ionization transients, temporal variations in pixel dark current and other effects. Because images are summed on-board, the ionization transients (i.e. cosmic ray like events) are scrubbed before summing on-board as is done on SECCHI/HI.

EMI/EMC The mission has very high EMI/EMC requirements. This normally affects remote sensing experiments via requirements on mechanical motors to move shutters, filter wheels, etc. The only mechanicm in SoloHI is a one-shot door, and does not have this problem. However, the variable instrument heater power consumption ultimately places a variable demand on the solar array, which could then possibly affect the sensitive *in-situ* instruments, e.g. the magnetometer (MAG). The heater-power issue is present in both the operational and survival heaters, and was mitigated by a combination of software and hardware solutions. A software control algorithm was added to manage the cycling of the various operational heaters to ensure that the on/off transitions do not exceed the requirement of transitions in current draw of 100 mA. The survival heaters are controlled by thermostats and operate when the SoloHI is powered off and thus are unable to be controlled by instrument software. Each survival heater was split into a trim and a bias heater. The trim heater cycles frequently to maintain the temperature above the survival temperature but draws less power than the 100 mA requirement. When the trim heater is unable to maintain the desired temperature, the bias heater is powered on, by ground command, to bias the temperature higher so that the trim heater can again maintain the survival temperature. In the current orbit scenario, the bias heater is not needed.

Contamination Sensitivity SoloHI is very susceptible to contamination from dust particles on the edges of the baffles and the lenses but is insensitive to contamination from organic compounds. However, SoloHI is in the discharge path of the propulsion jets that control the orbit and the attitude of the spacecraft. We were concerned that the accumulation of droplets could change the thermal properties of the Multi-Layer Insulation (MLI) and radiant cooling plates and thereby affect the operating temperature of the instrument, the electronics, and the APS detectors. This potential contamination source was eliminated by the spacecraft placing baffles in front of the propulsion jets on the spacecraft to block the outflow impinging on the SoloHI instrument.

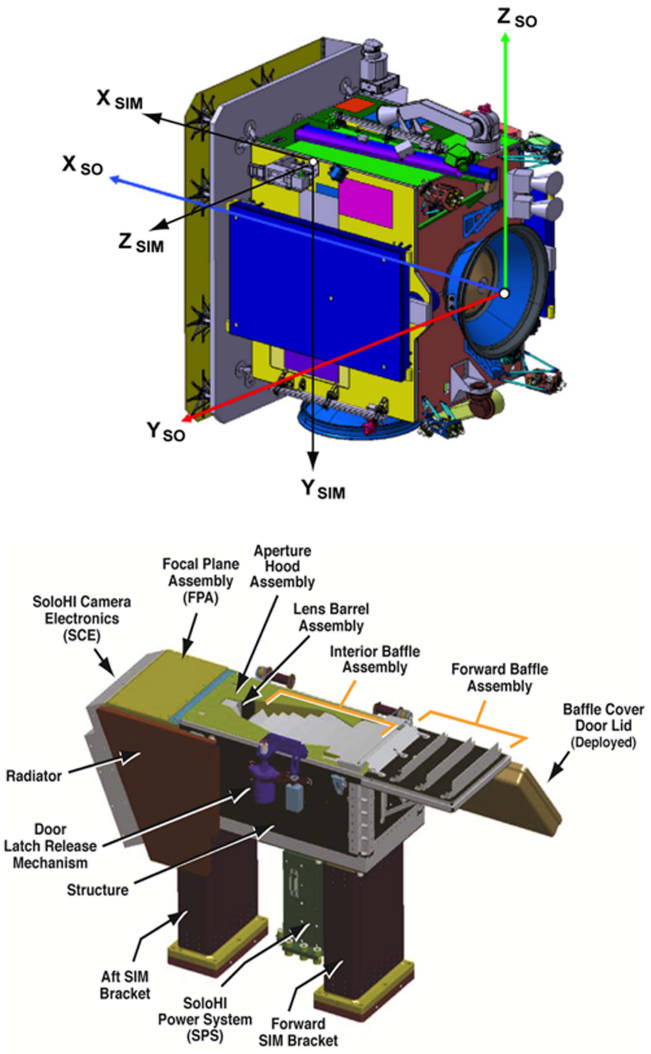

Fig. 6. Top: SoloHI accommodation on the Solar Orbiter spacecraft and reference systems. The SIM physical reference frame (subscripts SIM) with respect to the Solar Orbiter mechanical reference frame (subscripts SO).Bottom: SoloHI Instrument Module (SIM) and SoloHI Power System (SPS) and subassemblies.

4. SoloHI Instrument Design

4.1. Optical Design

The SoloHI telescope is a relatively simple design with a single lens assembly which together with the detector (see Section 4.6) form the focal plane assembly (FPA), described in Section 4.4.2. For SoloHI, direct illumination from the Sun is blocked by the heat shield. The baffles are designed to minimize the stray light entering the entrance aperture from various sources. The heat shield, one RPW antenna, and the solar array all either diffract or reflect light onto the instrument.

4.2. Lens Barrel Assembly

The SoloHI lens barrel assembly is a five-element wide angle design fabricated by Jenoptik. The lens design was optimized to maintain optical performance over the large 40° FOV and minimize stray light from scattering. A summary of the SoloHI optical parameters is shown in Table 2. Thermal and radiation requirements were incorporated into the design. Figure 7 shows

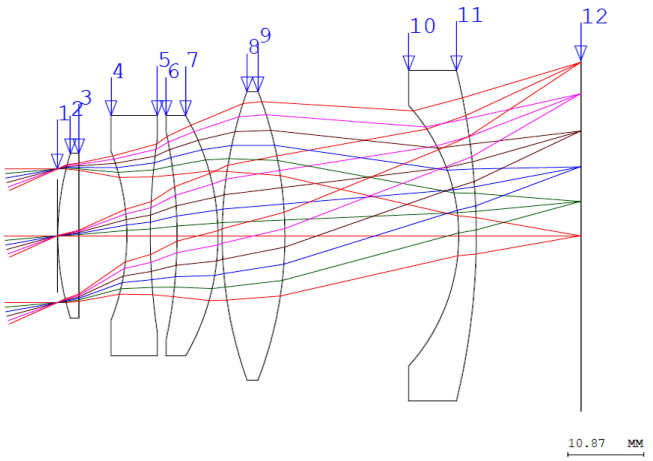

Fig. 7. Lens element layout and ray-tracing. The lens surfaces are indicated by the number along the top for the 5 elements. Surfaces 1 and 12 are the front lens plane and the focal plane, respectively.

the lens layout and ray-tracing. The resolution is optimized for the 7.5 $R_\odot$ solar distance, to satisfy the science requirement for observing the shocks, or density power spectrum in the corona, or SIR boundaries. The bandpass is set by using a long and short wavelength cutoff filter deposited on lens surfaces 7 and 9 respectively.

Figure 8 is a plot of the measured bandpass of the flight lens. The other lens surfaces are coated with an anti-reflective coating to maximize the throughput and minimize the ghosting. Ghosting performances have also been taken into account in the lens optimization by maximizing the image area of second order ghosts due to bright planets and stars. The first element of the lens uses radiation tolerant glass, the concept used for SOHO/LASCO, which has been in space for over 22 years with an average degradation of about 0.5%/year (Thernisien et al. 2006; Colaninno & Howard 2015). The lens barrel is made of titanium (Ti6Al4V), which makes the design almost insensitive to temperature variation, from room temperature to predicted operational temperature of −45°C. The off-axis rejection is maintained by using absorbing coatings and sizing of the lens retainers. The bandpass from 500 to 850 nm is wider than SECCHI/HI-1 which was from 550 to 650 nm. This difference enables SoloHI to gather significantly more photons than SECCHI/HI-1. The HI-1 had the same bandpass as the SECCHI/COR2 to ensure that they would have the same photometry, so that we could better follow structures from the COR2 into HI-1.

Due to the presence of the forward baffles, whose function is described in the next section, the image is vignetted all along the inner edge of the FOV, from approximately 5.4° elongation to 9°. The profile of the vignetting is shown in the bottom panel of Figure 8, from the theoretical boresight (25° elongation from the Sun center) to the inner edge (5° elongation). Natural vignetting of the lens is also present and follows a cosine^3 law with the field angle.

4.3. Stray-light Rejection

Baffle definition and position There are four sets of baffles - each serving a specific purpose.

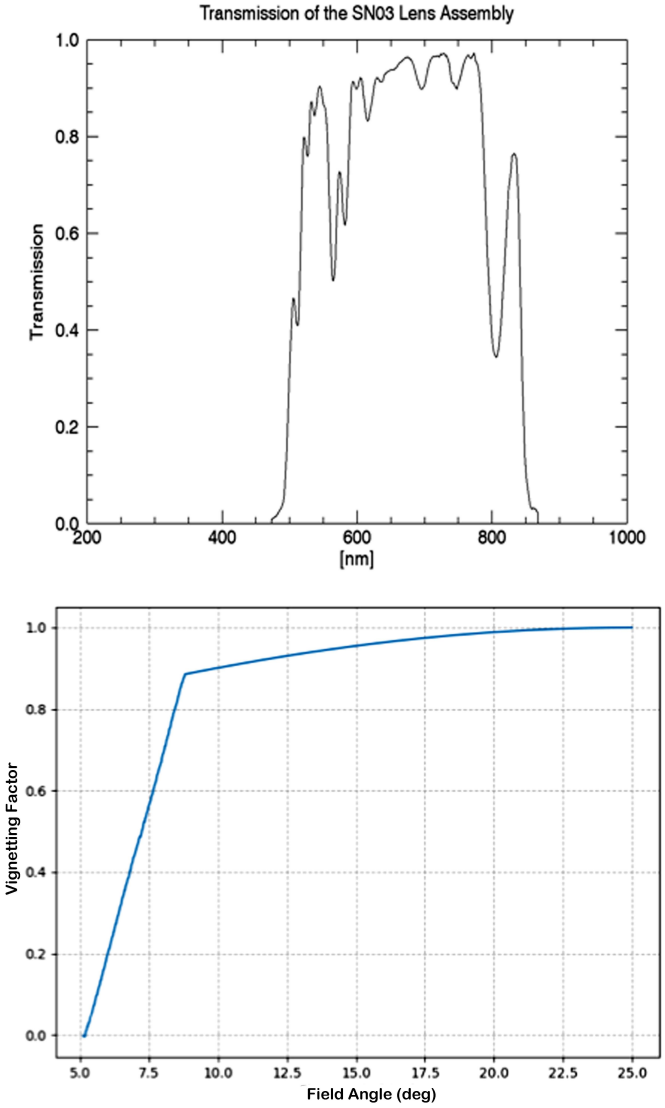

Fig. 8. Top: Bandpass of the flight lens (SN03), measured by Jenoptik. The bandpass is defined by a combination of a short pass and long pass coatings applied to surfaces 7 and 9. Bottom: Vignetting factor versus the field angle, from the inner field of view edge (5.4°) to the boresight (25°). The inner FOV is vignetted by the forward baffles from 5.4° to 8.8° and follows a $\cos^3\theta$ law.

1. Forward baffles: a set of 5 baffles, labeled F1, F2, F3, F4, and I0 on Figure 9, which block the direct sunlight and the subsequent diffraction from entering the telescope entrance aperture. The edge of the spacecraft heat shield is the first baffle in the system. The I0 baffle is not labeled in the figure, but is the dark horizontal line just after the F4 vertical baffle.
2. Interior baffles: a set of 9 baffles each pointing to the light-trap. The telescope aperture only sees the bottom surface of these baffles, so that any stray-light source above the SIM will have to bounce twice before entering the telescope aperture, thereby increasing the rejection of the stray-light source.
3. Aperture light trap: a set of 2 baffles, labeled AE1 and AE2, on Figure 9. Their role is to trap the residual diffracted sunlight coming from F4 and the reflected stray-light coming from the top of the interior baffles.

Table 2. Optical design parameters

FOV	40° x 40°, limited to Ø48° in the detector corners
Number of lenses	5 elements
Aperture	16mm x 16mm square with rounded corners Ø19mm
Imaging area (Measured)	38.84mm transverse x 40.12mm radial
Focal length(theoretical)	55.9mm
Plate scale (theoretical)	0.971mm/deg at 0° field; 1.082mm/deg at 20° field
F/# (Theoretical)	3.48
Spectral range (measured)	500nm – 850nm
Resolution (measured)	1.3' [arcminute], at full detector resolution.
Boresight/nominal pointing	25° elevation from Sun center
Inner FOV cutoff (measured)	5.4° fully vignetted; 9.30° fully unvignetted

4. Peripheral baffle. Not shown on Figure 9, the peripheral baffle is a plane that goes on top of the interior baffles. It cuts into the FOV of the telescope, blocking the direct view of the telescope aperture of the spacecraft heat shield.

Diffracted stray-light The design of the forward baffles (Figure 9) is based on the SECCHI/HI baffle design (Socker et al. 2000; Halain et al. 2011), however, in this case the edge of the spacecraft heat shield is used as the first baffle, and then the four baffles on the SoloHI reduce the diffraction from that first edge to an acceptable level. The right panel of Figure 9 shows the diffraction reduction by the various baffles. Using only one baffle to totally block the direct sunlight is not sufficient to achieve the stray-light level needed to observe the faint solar corona, which is more than 10 orders of magnitude dimmer than the solar disk brightness. Each baffle provides roughly 3 orders of magnitude attenuation of the diffraction, so at least 4 are needed to achieve the requirements. For robustness and to account for fabrication, alignment tolerances, and spacecraft off-pointing, one more is used in the SoloHI design. Note that F4 does not participate in the diffraction attenuation but is there to provide a light trap effect in conjunction with the I0 baffle.

The diffracted stray-light requirement at 0.28AU ranges from $1x10^{-10}$ $B_\odot$ at the inner FOV to $1x10^{-13}$ $B_\odot$ at the outer FOV . Measurements of the diffraction performances in space-like conditions were performed on the flight instrument in the SCOTCH vacuum chamber at NRL. No spacecraft heatshield was present during this test, so a model of the diffraction from that single edge had to be added to compute the expected stray-light levels in flight. The test showed that the requirements were met.

Reflected stray-light We define the reflected stray-light as the fraction of the sunlight that is reflected or scattered off the structures of the spacecraft, then illuminates the SIM and finally ends up on the image plane. Three structures on the spacecraft have been identified as sources of such stray-light: 1) the solar array, 2) the heat shield, and 3) an RPW antenna. Raytracing analysis showed that the dominant contribution comes from the solar array, while the two others have more modest contributions.

The solar array (SA) is an 8.2m high by 1.2m wide structure, fully illuminated by the Sun, and stands 1.5m in the back and 1.0m to the left of SoloHI when looking at the Sun. This is a large light-reflecting area. Viewed from the SIM perspective, the SA represents approximately 0.6sr. The amount of light that

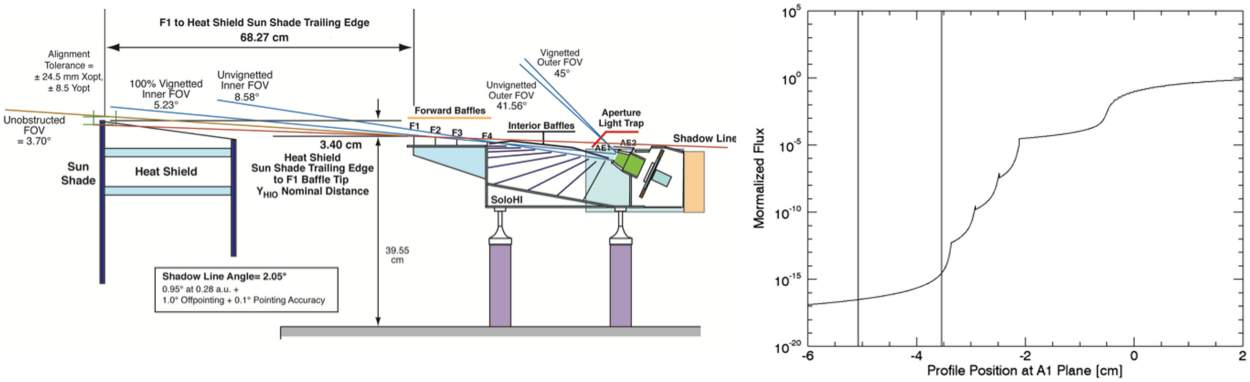

Fig. 9. Left: Definition and position of the optical baffles, with respect to the SIM and spacecraft heat shield. Right: Predicted diffracted irradiance at the SIM telescope entrance aperture (A1). This is in the nominal case heat shield alignment and spacecraft pointing (+1.1deg pitch down), at 0.28AU. The labels above the curve show where the attenuation provided by each baffle occurs. The vertical lines pointed by the A1 label show the dimensions of the telescope aperture

the SA will scatter towards the SIM depends on three things: the geometry of the SA, the bidirectional reflectivity distribution function (BRDF) of the array, and the steering angle of the array relative to the Sun direction through the orbit. All these parameters were provided by ESA. However, we measured the BRDF of the flight SA to validate the stray light model.

To predict the expected amount of stray-light due to the SA while in flight, ray-tracing software was used. The model included the SA, the SIM with all the forward and internal baffles, the lens and lens barrel, and the detector. The SIM model was based on the CAD model of the instrument, and all the optically relevant parts were identified with their expected optical properties.

Optical testing of a flight like SIM baffle mockup built early in the development phase allowed the correlation of the stray-light model to the observations (Thernisien et al. 2018). During integration of the flight model (FM) instrument, reflected stray-light tests were also done. The data collected showed a good agreement with the stray-light model. An example is shown on Figure 10. Stray-light requirements were then verified by an end-to-end run of the model with flight conditions and factoring in the SA.

4.4. Mechanical Design

SoloHI adopted a modified protoflight model (PFM) philosphy, meaning that there was no qualification model (QM) of the full instrument. A QM was used to ensure the design the focal plane assembly which went through two iterations before the vibration and thermal requirements were satisfied. The flight instrument was vibrated to qualification levels for flight durations.

4.4.1. Instrument Enclosure

The SoloHI instrument enclosure (Figure 11) directly supports the external baffles and encloses the interior baffle structure. The FPA mounts directly to the rear of the enclosure. The mounts to the side and protects the optical surfaces. The top perimeter of the instrument enclosure is machined to incorporate a stepped ledge to accommodate a labyrinth seal with the door cover. The mechanical design of the enclosure meets high-G structural loading, alignment stability, FOV, contamination control, and thermal performance. The instrument enclosure is fabricated from composite honeycomb panels of CFRP (M55J) facesheets, 5056 Aluminum Core, and adhesive corefill. The panels are joined with 'C' (channel) clips and 'Y' bracket clips fabricated from Ti-6Al-4V. The clips are structurally bonded to the enclosure walls with a blended mixture of EA9394 and EA9396 adhesives. Click bonds are implemented in the clips to accommodate fasteners for attaching the walls together. Ti-6Al-4V inserts are potted into the panels for integrating components.

4.4.2. Focal Plane Assembly (FPA)

The SoloHI Focal Plane Assembly (FPA) is shown in Figure 12 with the lens assembly mounted. The FPA includes the APS detector package with Detector Interface Board (DIB), the Detector Readout Board (DRB), the SoloHI Camera Electronics (SCE) and the thermal strap to the radiator that provide passive cooling for the detector. The FPA housing is comprised of Ti-6Al-4V walls. The housing assembly interfaces to the SIM structure with a Ti-6AL-4V bulkhead bracket through structural, titanium (Ti-6AL-4V) clips. Internal FPA components are accessible through separate, removable walls. The lens barrel assembly is mounted directly to the FPA via a bulk head interface that defines the optical axis of the telescope. The FPA structure positions the detector with respect to the telescope mounting interface. The APS detector is supported in a clamshell mount to accommodate de-center alignment. Focus alignment of the lens barrel to the detector and overall position alignment of the telescope (lens barrel – detector system) to the F1 baffle is accommodated with shim spacers. Focus and position alignment of +/- 2 mm is accommodated in the assembly. The clamshell assembly accommodates +/- 1.6 mm for de-center correction. The close proximity of the telescope assembly to the APS detector imposed a challenging requirement on the thermal design in that the telescope needed to be maintained no colder than about -45°C, whereas the APS needed to be cooled to no warmer than -55°C. The clamshell mount accomplished that objective.

4.4.3. Baffles

All baffles are fabricated from aluminum and are optically coated black with either black anodize, Laser Black, A382 or Z307

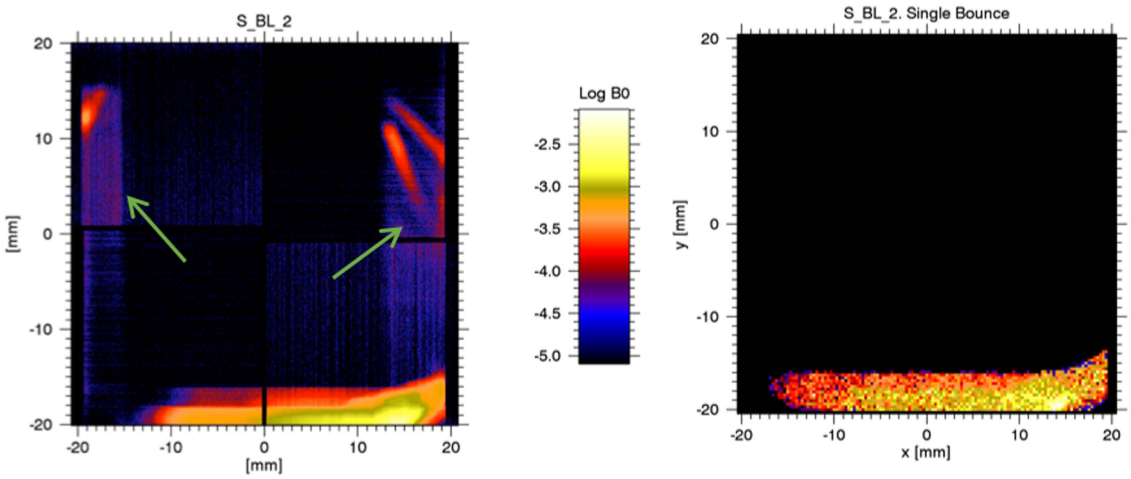

Fig. 10. Example of data image (left) compared to the stay-light model simulation (right). Features pointed by the 2 green arrows on the left panel are part of the scene. They are not instrumental features.

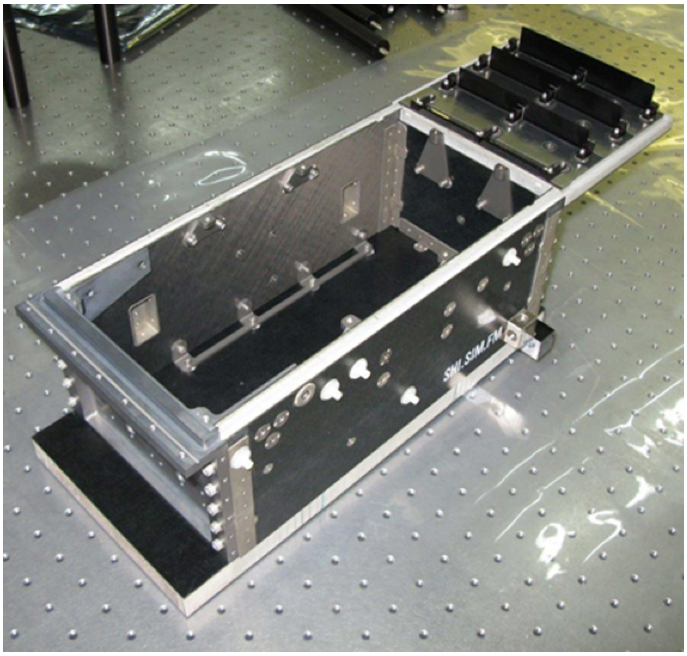

Fig. 11. SoloHI Instrument Module (SIM) Enclosure.

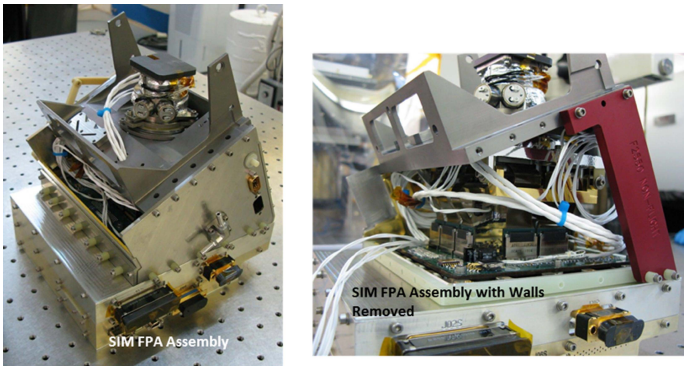

Fig. 12. SIM Focal Plane Assembly. The left figure shows the final flight configuration, with the lens assembly at the top and the camera electronics enclosure at the bottom. The right figure shows the assembly with the walls removed and a non-flight red bracket to temporarily hold the clamshell mount in the proper position.

paint depending on location and purpose. The forward, peripheral, and light trap baffles individually attach to the SIM structure via baffle mounts. The interior baffles are installed in aluminum side walls along with a front, bottom, and back cover to form an integrated unit. The interior baffle box unit is integrated into the instrument enclosure with a front flexure and two aft mount pins to reduce thermal strain and maintain baffle orientation alignment. To facilitate initial alignment measurements with the interior baffles, specifically with the no-touch Laser Black baffles, a red anodized assembly was built to characterize initial alignments and evaluate shifts due to variance in coating.

Forward and light trap baffle horizontal and vertical alignment accommodation is +/-0.5 mm. The interior baffle box orientation alignment is accommodated with spacer shims underneath the flexure surface to adjust as a system with respect to the light trap baffles. To meet the forward baffle alignment requirements, the forward ledge support braces originally fabricated from Ti-6Al-4V for the qualification unit required replacement with Invar braces for the flight unit.

4.4.4. Door

The cover door provides a protective barrier for the baffles, telescope, and opto-mechanical hardware from contamination during the S/C integration activities, the launch environment, and the initial cruise phase of the Solar Orbiter mission. After the spacecraft reaches the nominal science orbit, the cover door will be released utilizing a one-shot door mechanism. The cover door is preloaded against two cup-cone joints to prevent door chatter through the Solar Orbiter launch environment. An Ejection Release Mechanism (ERM) is used to release the door. The preload set on the ERM for launch is controlled via a Strainsert instrumented bolt in combination with a Belleville washer. The cover door is driven to its door open position using two torsion springs and a kickoff spring and is held open by the prevailing torque margin in the torsion springs at 225° relative to its door closed position. The mechanisms subsystem also incorporates a door closed telemetry switch, which furthermore acts as the kickoff

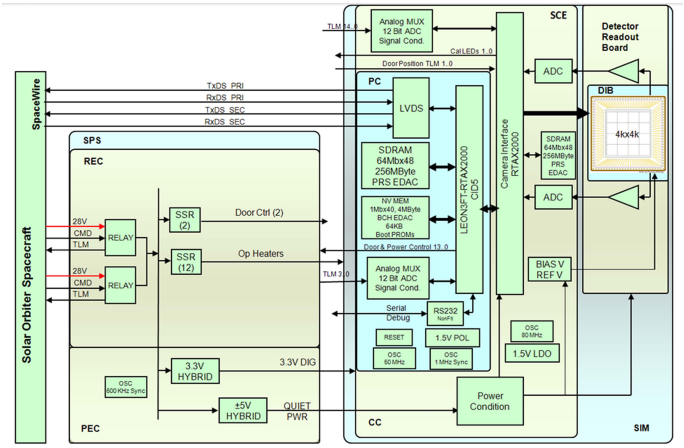

Fig. 13. SoloHI Electrical Block Diagram.

spring and two door open telemetry switches. A door lid over-travel stop is used to constrain the maximum angular position overshoot beyond the open position. In addition, a door lid compliant stop is used to attenuate the impact energy imparted to the SIM, when the door lid strikes the door lid over-travel stop.

The SoloHI door is fabricated from T-300 satin weave fabric. It is post machined to form a lip to create a labyrinth seal with a stepped ledge in the enclosure panel. The seal allows for venting while implementing a convoluted path for contaminants. In addition, two ascent vents with sintered metal filter discs are installed in the door.

4.4.5. Instrument Mounts

To align the optical axis of the SoloHI with the Solar Orbiter heat shield the SIM is raised off the spacecraft deck with instrument mounts. The S/C interface brackets are fabricated from M55J laminate with T-300 overwrap and Ti-6Al-4V fittings. The composite portions of the two mounting brackets are rectangular tubes. The design of the mounts required a lightweight isolation system that could position the instrument enclosure off the deck nearly 220 mm to meet the F1 baffle to heat shield positional requirement, maintain alignment, meet a primary instrument frequency mode above 140 Hz, and withstand high vibration loads. Between the mounts and the spacecraft deck are Ti spacer and shim stack. The height of the spacer and shim stack was determined based on measured alignment of instrument with the spacecraft reference frame after final installation of the Solar Orbiter heat shield.

4.5. Electrical Design

The SoloHI electrical design (Figure 13) consists of five subsystems: the SoloHI Power System (SPS), the Processor Card (PC), the SoloHI Camera Electronics (SCE), the Detector Readout Board (DRB), and the Detector Interface Board (DIB). Each component comprises several subsystems, which we describe briefly below.

To meet the requirements for mass and power, SoloHI chose a light weight, lower power CPU the LEON3FT with 20 MIPS. RTEMS 4.10 was chosen as the real time operating system, since a C++ compiler and board support package for the LEON3FT was available. Using the RTEMS and C++ combination allows the same basic design of the heritage STEREO SECCHI software to be used. There is a near one to one correspondence of system calls between VxWorks used with SECCHI and RTEMS for SoloHI. To lighten the CPU load, some camera operations (starting/stopping the camera) and time intensive image processing functions (pixel summing, image summing, truncation, and cosmic ray scrubbing) were incorporated into the camera FPGA. On SECCHI, these processes are run by the SECCHI CPU.

4.5.1. Processor Card

The SoloHI processor card is based on an Aeroflex Gaisler LEON3FT processor with support for 256MB of SDRAM, 64kB of PROM, and 4 MB of non-volatile MRAM. The LEON3FT is implemented on an RTAX2000 FPGA running at 25 MHz, which results in 20 MIPS. The SoloHI processor is based upon the configuration identification 5 (CID5) COTS with modifications. The science data, HK telemetry, and telecommands are provided via nominal and redundant SpaceWire links. Control of operational heaters and one-shot door is provided via a GPIO connection. Aeroflex Gaisler provides COTS driver support for memory controllers, SpaceWire, and GPIO. The Aeroflex Gaisler modifications for SoloHI are: a switchable single SpaceWire core instead of multiple cores, an additional GPIO interface, and a custom SoloHI camera interface.

4.5.2. SoloHI Camera Electronics (SCE) and Camera Card (CC)

Figure 14 gives a block diagram of the SCE-CC. The CC takes the analog video signal from the DRB and digitizes the intensity information to 14 bits. It sets the offset and gain parameters to the ADC, to allow for shifts due to radiation damage. The CC is a smart camera with 256 MB of memory and is capable of doing simple image processing. The three functions provided in the camera FPGA are cosmic ray scrub with bias subtraction, pixel binning and image summing with 16-bit packing, and truncation. Images are stored in the camera memory and then transferred to the LEON3FT processor for further image processing and image compression before being sent to the spacecraft. The LEON3FT will manage the camera buffers in both the CC and the PC. The camera can read out full images as well regions of interest (ROI) on each die depending upon the microcode and parameters loaded to its registers. The CC also controls the calibration LEDs to provide a stimulus to the APS during AIT activities.

The camera gets its instructions to take images from sequences of binary coded instructions called “microcode.” The microcode is loaded to the camera and then commanded to begin executing. Individual processed exposures are then sent by the camera to the LEON3FT processor in a continuous loop until commanded to stop. Each observing program has a unique microcode. Storage for up to 128 microcode sequences is available, and we are currently using 32 slots. Scene readout is done by individual detector, and more specifically by row. There are two readout chains so two readouts can be done at once, one using the outer detectors (top) and one using the inner (bottom) detectors. This also allows different settings for the top two and bottom two detectors. The readout is controlled by camera microcode that is uploaded to set the timing of each readout chain. The microcode reads register values to set parameters such as exposure time and image size. Since the APS pixels are row and column addressed they can be read out with different timing, i.e. for a single detector one block of rows can be read out at a different frequency than another block, within

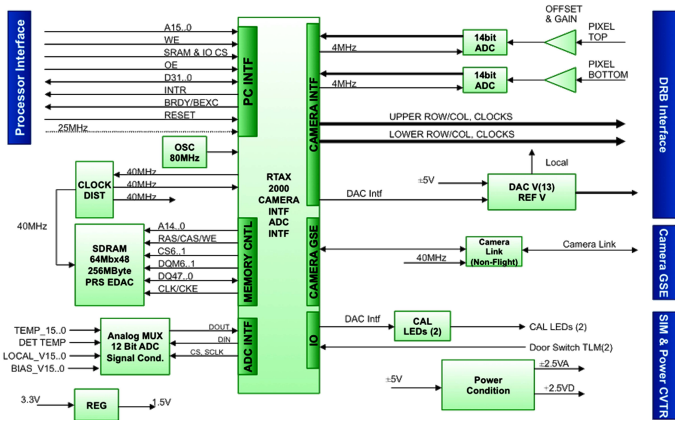

Fig. 14. Block Diagram of the SoloHI Camera Electronics (SCE) Camera Card (CC)

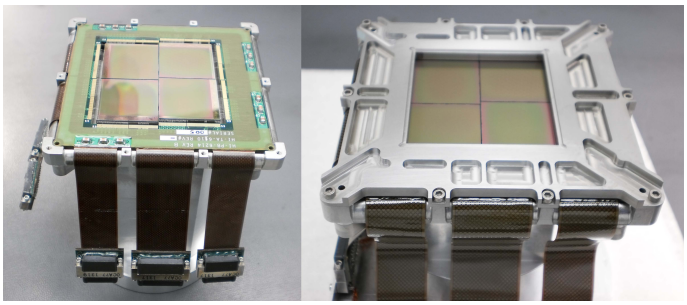

Fig. 15. SoloHI flight Active Pixel Sensor consists of four abutted die mounted in a windmill configuration. Left: detector photograph without the mask showing the four die, the detector interface board and the wirebonds. Right: the complete assembled device

the readout timing constraints of top or bottom and one row at a time.

4.5.3. Detector Interface and Readout Boards (DIB/DRB)

The four APS detector die are mounted to the DIB (Figure 15, left), which interfaces through a rigid-flex cable to the DRB. Printed circuit traces on the DIB combine the same signals from the four die, into a single signal onto the rigid-flex cable. This greatly reduces the number of wires in the rigid-flex cable and also reduces the heat transfer from the DRB to the APS.

The DRB multiplexes the various video outputs from the APS and conditions the video signals to match the requirement for the ADC on the CC.

4.6. Active Pixel Sensor (APS)

The SoloHI detector will provide panoramic images of the inner heliosphere. The 5T pixel design and device architecture was specifically developed to meet the Solar Orbiter mission requirements and SoloHI photometric and imaging requirements. Details of the APS architecture and development are documented in Janesick et al. (2010, 2013) and Korendyke et al. (2013). With an image size of 3920x3920 pixels, the device is one of the largest format APS detectors to be fully qualified for space. A photograph of the flight device is shown in Figure 15 in two stages of assembly. The left side of the figure shows the four die, the DIB and the wirebonds and the right side (with a 180° rotation) shows the fully assembled configuration with the molybdenum cover attached. Each die has two rigid flex cables connecting the DIB to the camera electronics. Three of the eight rigid flex circuits are readily visible in both images. The mechanical package is molybdenum, which has a coefficient of thermal expansion well matched to the APS. Molybdenum was also found to be stable, machinable and non-ferrous. The gap between detector imaging areas is <1mm with 0.88mm being typical.

Figure 16 is a schematic that shows the pinwheel configuration of the 4 die in the mosaic. The solar disk would be to the right and increasing heliocentric distance is from the right to left. The die positions are arbitrarily numbered, 1 to 4, in a counterclockwise direction, beginning in the lower right. The horizontal and vertical lines show the direction of the rows of each of the direction. The red lines at the outer edges of each die indicate the locations of the 10 opaque rows and columns. The opaque pixels enable a determination of the bias voltage and dark signal in each exposure. The corner between those lines is the (0,0) pixel. Putting that pixel to the lower left, readout occurs from that pixel along the bottom to the right. The optical system FOV is the circle around the die. The SoloHI die were produced on the Jazz Semiconductor, Inc. foundry imaging line. There were 44 individual die per wafer with a total of 25 fabricated wafers. Several processing variations were incorporated into the fabrication run. The SoloHI die were selected from wafers 11-15 of the lot run. The readout frame is along the left and bottom of the die. The individual pixel controls are located on the left side; pixel transistors in an individual row are controlled and sequenced together. The column controls and capacitors to store the individual pixel voltages are located on the "bottom".

A schematic of the 5T SoloHI pixel is shown in Figure 17. The photons are collected within a large pinned photodiode which occupies roughly 63% of the pixel area. Pixel controls are implemented with five transistors, (reset, gain control, transfer gate, source follower and row select). The sense node is separated from the pinned photodiode with a transfer gate. The pixel architecture allows separate reset of the sense node from the pinned photodiode as well as "snap" mode operation. The low/high gain is realized a metal-insulator-metal (MIM) capacitor controlled through a dedicated transistor. The capacitor is in parallel with the sense node. The source follower and row select transistors are used to transfer the sense node voltages to the readout frame. During correlated sample and hold (CDS) readout, the sense node voltage reset voltage for each pixel is transferred and stored on a capacitor in the readout frame. The difference between the reset and the photo-electron voltage is accessed through one of the four die readout ports and digitized with an off-chip analog to digital converter. The progressive scan/rolling curtain shutter allows photons to be collected during device readout and minimizes the amount of time voltages are stored on the sense node.

The device is front side illuminated with an estimated 63% fill factor giving an average visible quantum efficiency of 32%. This quantum efficiency is sufficient to record a high quality scene of the inner Heliosphere. The device will be operated with a rolling curtain shutter and, therefore, does not require a shutter mechanism. Although the device architecture supports pixel readout rates of up to 4MHz through a total of 16 readout ports distributed across the four die, for SoloHI, the device will be operated with a readout rate of 2MHz with two independent readout chains, one for the upper two die and the other for the bottom two die. Table 3 describes the photometric and imaging characteristics of the device. The image in Figure 18 of a resolution target, taken on a single die at -65°C gives a subjective indication of the

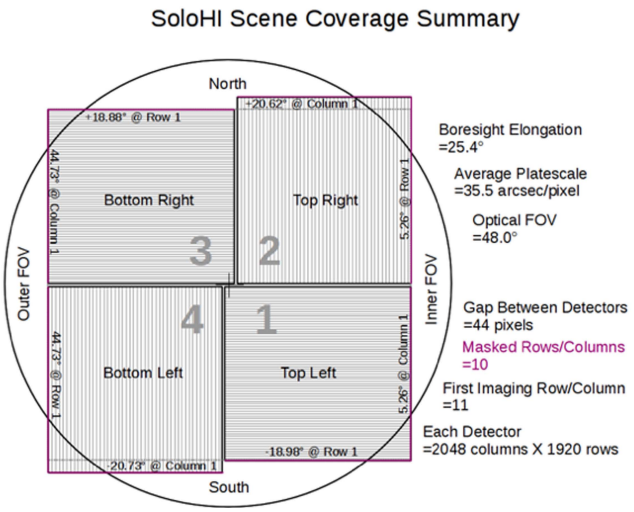

Fig. 16. Schematic of the orientation of the APS with respect to the instrument FOV. Each die is oriented in a pinwheel configuration. The red lines on the corners of each die show the locations of the 10 rows and 10 columns that are covered with an opaque metal coating. The ground processing software combines the separate images from each die into a single mosaic of the full SoloHI image.

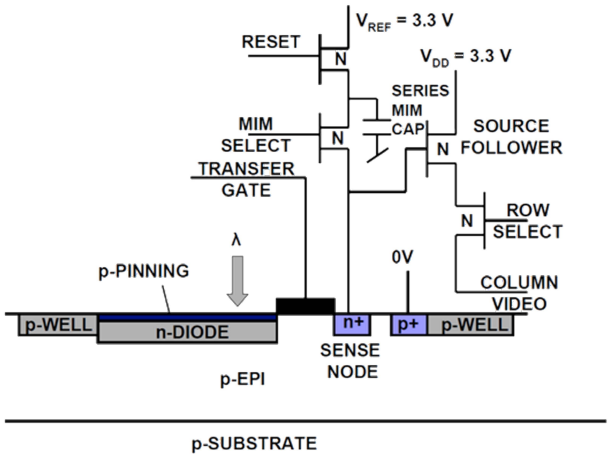

Fig. 17. SoloHI 5T Pixel Architecture

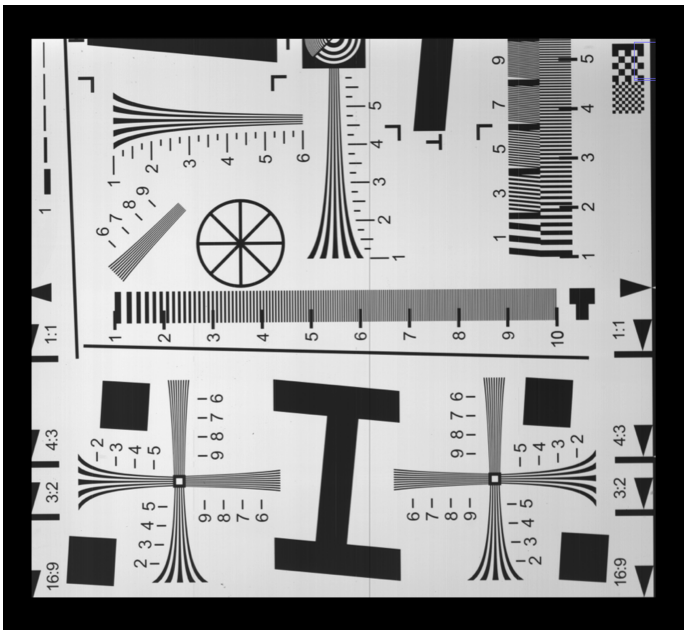

Fig. 18. Image of Test Pattern Projected onto a Single Die. The image was taken with a single die at -65°C.

Table 3. SOLOHI APS Detector Performance Capability

Parameter	Capability
Overall Format	3920 x 3920 pixel area, 10 σm
Die Format	1920x2048, 10 micron pixels, 10 row and column pixels are opaque
Linear Full Well	>86400 electrons low gain >19200 electrons high gain
Read Noise Through Image Chain (BOL)	35.1 electrons low gain; 5.8 electrons high gain
Dark Current	<0.3 e/pix-sec (BOL) for long exposures <2 e/pix-sec (EOL) for long exposures
Quantum Efficiency	32% average over 480-750 nm
Pixel Readout Rate	4 MHz per readout port. 2MHz flight rate
Imaging Performance	Device MTF>80% of the ideal value
Operation Mode	Both snap and rolling shutter (progressive scan) mode enabled
Redundancy	Top and bottom half of detector mosaic with separate readout chains Each die is read through four individual ports.

good imaging performance. Analysis of the MTF data showed that the detector had imaging performance within 80% of an ideal 10 micron pitch detector. The APS detector performance was thoroughly characterized in a series of tests conducted at SRI (Huntington Beach), SRI (Princeton) and NRL with three different sets of drive electronics. The SRI (Princeton) testing was conducted using GSE electronics. The SRI (Princeton) electronics operated the device using four ports simultaneously with a readout rate of 4MHz/port. The NRL testing was conducted using a flight-like set of electronics with flight timing patterns. The SRI (Huntington Beach) testing was conducted at slower clock rates using a proven set of electronics with extensive test heritage. Across the board, the results were remarkably consistent which gave an extremely high level of confidence in the selected operating voltages, the general operation of the device and the overall expected performance. The combined data from the test sets were used to set the device operating parameters for the flight electronics and verify that the performance of the flight die and detector met the performance requirements. The read noise performance is shown in Figure 19 (left) for the two different gain modes of the device. To perform the measurements, a set of quiet electronics (noise≈2-3 electrons) was used. The median value of the high gain noise of 5.76 electrons is comparable to scientific CCDs. The linearity is also excellent. Figure 19 (right) gives the linearity response for 16 regions of 64x64 pixels across the die. The difference from the linear fit is given as the curved lines. For most of the range, the non-linearity is within +/-1%. Other tests included the conversion gain at each pixel, the quan-

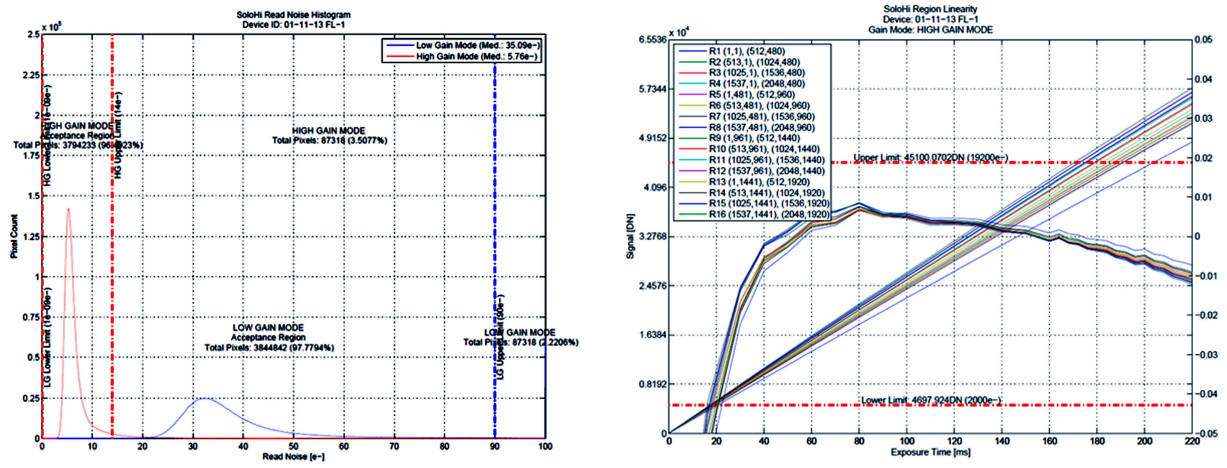

Fig. 19. Left: Read Noise Performance. The low gain mode histogram plot is in blue and the high gain histogram plot is in red. The requirements for the two modes is shown in the vertical dashed lines of the corresponding colors. The median value of the high gain noise is 5.8 electrons and the low gain is 35.1 electrons.Right: Linearity Response in High Gain. The linearity was computed within 16 regions. Each region is plotted as the total signal (left axis) vs the exposure time and the difference from a linear fit expressed as a ratio to the total signal (right axis). The horizontal dashed lines give the lower and upper limits of the ratio requirements

tum efficiency, the charge transfer efficiency, various voltages and currents.

4.7. Thermal Design

SoloHI (SIM and SPS) has an isolated thermal interface with the spacecraft and is designed to be insensitive to temperature changes at the spacecraft mounting interface and its external environment. The conductive flux with the spacecraft shall be between -1 W to +1 W. (A maximum of 1 W will flow from the spacecraft to the isolated payload in the cold survival case. A maximum of 1 W will flow from the isolated payload to the spacecraft in the hot survival case.)

When SoloHI is operating, the SIM is completely in the shadow of the Solar Orbiter heat shield even at the worst extreme 1.0° offpointing from Sun center at orbital perihelion, so there is no direct solar load. The SoloHI instrument has been designed to operate and continue to capture images that satisfy the science measurement requirements for off-points from Sun center of $\leq 1.0°$. In addition, the SoloHI instrument will survive when the Solar Orbiter spacecraft off-points by $\leq= 3.5°$ from Sun center steady-state and by $\leq 6.5°$ from Sun center for 50 sec. The SoloHI instrument does not need to perform science operations for these off-pointing failure cases, and SoloHI autonomy rules may request that the SoloHI instrument be powered off if the SoloHI electronics or optics exceed the autonomy rule temperature limit.

The SIM conductive interface is defined by the temperatures and linear thermal conductance across the SoloHI flexure mounts. The radiation interface is defined by the temperature on the spacecraft side of the payload interface, the radiation coupling between the spacecraft and payload, and between the payload and deep space.

The SIM cools its APS detector to its operational temperature using a passive radiator that radiates the detector's heat (and parasitic heat) to deep space. The expected temperature of the detector is -65C with a ± 10 C uncertainty. The cooling of the APS to <-55 C is accomplished by conducting the heat from the APS to a radiator on the -YSIM side of the SIM. The radiator is coated with Z93 white paint to passively radiate the heat to deep space and is sized to achieve a temperature <-55 C. Components around the APS radiate heat onto the APS, which must also be considered in the sizing of the radiator. The lens assembly, being so close to the detector is also cooled and has heaters attached to maintain the lens temperature above its minimum thermal requirement.

4.8. Flight Software

SoloHI is the latest in a series of coronagraphs and heliospheric imagers built by the NRL. The SoloHI flight software has heritage from the STEREO SECCHI telescope suites, NASA Small Explorer (SMEX) satellites, and the SOHO LASCO/EIT telescopes. The starting point for the SoloHI flight software (Figure 20) was the SECCHI flight software, which satisfied many of the basic scientific requirements for space coronagraphs.

The requirements for basic functions such as telemetry, command handling, health and safety, and heater control are generally very similar from instrument to instrument. Modifications of the software requirements were needed primarily because of different specific hardware (CPU, camera, heater, thermistors) and spacecraft-interface requirements. The flight software is designed as many separate tasks with the advantages of being able to debug tasks separately and to load/reload separate tasks when a problem occurs and a revision is necessary. The software tasks can be updated in the Non-Volatile Random Access Memory (NVRAM) as individual files. The tasks communicate with each other using a software bus. Separate tasks handle the various software functions such as communicating with the spacecraft, instrument health, sequence control, housekeeping, image scheduling, camera control, and image processing.

The camera software and microcode work together to read out an image. The LEON3FT software sets up the camera FPGA parameters specifying where an image goes in the camera memory, how to process the image, and where to put the output image. The camera FPGA can do many image processing func-

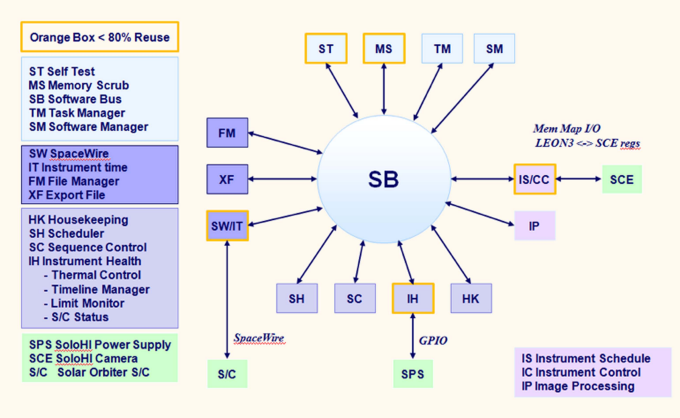

Fig. 20. Software Tasks and Heritage. Most of the tasks were heritage, except for the boxes with the orange border which had >20% rewrites.

tions including summing of multiple images, binning 2x2, 4x4, or 8x8 pixels, truncation, and cosmic ray scrubbing. The camera can handle up to four different images, each with different image processing parameters, from each detector for a total of 16 images at once. The major resources to be managed are the camera memory and timing of the images. It is quite possible to take images faster than they can be processed so any new microcode must be carefully tested. The microcode generates a sequence of images that is predictable and the LEON3FT software uses this information to set the registers in the camera FPGA.

The finished image is then transferred from the CC to the LEON3FT for final image processing and compression. The LEON3FT image processing steps include managing the on-board storage by enforcing a data quota, generating low latency images or subregions, masking of images and doing either lossless (Rice; Rice 1978) or lossy (H-compress; Wang et al. 1998) image compression, and generating the image header. Other functions include calculating a bias image from the masked pixels of an image for the camera FPGA to use for bias subtraction, the generation of known diagnostic images and header only images.

The observing program schedules the time for the start of each image exposure. The schedule specifies all the parameters for the image and the data compression technique. The need to manage the on-board storage and enforce a data quota is due to the unknown degree of compression. The schedule is developed with an average compression factor, but that may underestimate the actual size of an image if there is something unusual, such as an energetic particle storm or a comet passage. This can increase the total storage requirement. The flight software will autonomously modify the observing program if the orbit quota is going to be exceeded. The quota is stored in the NVRAM and will be set to a value less than the real quota, to ensure the real quota is not exceeded.

5. Science Operations, Data Processing and Products

5.1. Description of Nominal Observations

Routine observations to meet the science objectives are nominally planned to occur during three remote sensing windows, each of ≈10 days duration. These windows are nominally centered on perihelion and the northern and southern latitudinal extremes for each orbit of about 170 days, i.e. 30 days each orbit. A standard image sequence takes a series of short exposures (<20 seconds), summing them to achieve the required integration time and signal-to-noise ratio. Each exposure is scrubbed for cosmic rays using techniques that were developed and used on SECCHI/HI before summing on board (Eyles et al. 2009). The instrument is operated primarily in a synoptic observing mode, and similar observations are conducted each orbit using preplanned schedule blocks uploaded in advance of each encounter. Special observations tailored to specific science objectives are conducted on selected orbits (e.g. close to the minimum perihelion or with favorable geometries of Earth or other missions). Data are stored on the solid state mass memory (SSMM) for later transmission to the ground. Due to the potential for a large lag, perhaps months, between the image acquisition period and their downlink, SoloHI generates a quick-look data product, that is downlinked in the low-latency channel, to demonstrate the proper functioning of the instrument and to provide a view into the structure of the corona to facilitate preliminary evaluation of the data being collected. The low-latency data are transmitted to the ground within the next 24 hours.

Figure 21 shows our candidate observing program designed to fulfill the science objectives for the first orbit in the nominal mission (Orbit 1). Many of the baseline science measurement requirements (including radial scene coverage, photometric accuracy, image cadence, and science observation days) depend on the instrument distance from the Sun. The data collected is a function of the heliocentric distance of the spacecraft – the further the instrument is from the sun, the lower the data rate downlinked and vice versa. This variation in the data rate is partly because the exposure times are much longer because the signals are much lower. The table shows, for each type of image, the pixel binning, the image size, both before and after data compression (DC), the image cadence, and the total data volume. The parameters have been defined for various ranges of heliocentric distances - perihelion, near-perihelion, far-perhelion, and then the northern and southern latitude extremes. The particular parameters will be chosen as appropriate for the three remote sensing windows.

The highest cadence observations are taken over a 36-hour period centered on perihelion. At larger distances from the Sun, the image cadence is reduced to satisfy the required photometric accuracy requirement. The observing program, including science data, housekeeping data, and CCSDS packet overhead, is constrained to fit within the SoloHI data volume allocation of 53.1 Gbits for each orbit.

Planning the observations depends upon the orbital parameters – i.e. the perihelion and aphelion distances and the orbital inclination – which change only after a gravity assist maneuver. Thus there are a small number of distinct orbits. Nominally the same set of synoptic observations will be taken during each orbit with similar orbital parameters. Many of the baseline science measurement requirements (including radial scene coverage, photometric accuracy and image cadence) are dependent on the instrument's distance from the Sun and the solar latitude for the SoloHI instrument. For this reason, the observing program for each orbit will be divided into five regions based on the instrument distance from the Sun:

- Region 1 (Perihelion): 0.28 to 0.29 AU
- Region 2 (Near Perihelion): 0.29 to 0.36 AU
- Region 3 (Far Perihelion): 0.36 to 0.42 AU
- Region 4 (Southern Out-of-Ecliptic): 0.42 to 0.50 AU
- Region 5 (Northern Out-of-Ecliptic): 0.50 to 0.70 AU

Observations near perihelion will focus on science objectives that benefit from higher spatial or temporal resolution. At this

		Field of View					Image Size (MB)					Data Volume (Gbits)	
Observing Region	Image Type	Radial	Trans-verse	Bin Size	Downlink Pixel Count (Mpixels)	Bit Depth	w/o DC	w/ DC	Image Cadence	Period (hrs)	Daily Image Count	Daily	Orbital
Perihelion 4 days	Full Frame	5° to 25°	40°	2 x 2	1.92	17	7.3	2.16	24 min	96	60	1.09	4.36
		25° to 45°	40°	2 x 2	1.92	16	7.3	1.32	30 min	96	48	0.53	2.13
	Inner FOV Subframe	5.8° to 7.68°	5°	1 x 1	0.10	14	0.375	0.062	0.3 min	12*	1200	0.62	1.25
		13.5° to 15.38°	5°	2 x 2	0.025	14	0.094	0.016	0.6 min	12*	600	0.08	0.16
		18.5° to 20.38°	5°	2 x 2	0.025	14	0.094	0.016	1.50 min	12*	240	0.03	0.06
	Radial Swath Subframe	5° to 25°	5°	2 x 2	0.25	17	0.97	0.29	6.0 min	48	240	0.58	1.15
		25° to 45°	5°	2 x 2	0.25	16	0.97	0.26	12.0 min	48	120	0.27	0.53
Near Perihelion 8 days	Full Frame	5° to 25°	40°	2 x 2	1.92	18	7.3	2.33	30 min	192	48	0.94	7.5
		25° to 35°	40°	2 x 2	0.98	15	3.8	0.44	30 min	192	48	0.18	1.43
		35° to 45°	40°	2 x 2	0.94	15	3.6	0.61	30 min	192	48	0.24	1.95
	Inner FOV Subframe	5.8° to 7.68°	5°	1 x 1	0.10	15	0.375	0.176	0.6 min	24*	600	0.33	1.31
		13.5° to 15.38°	5°	2 x 2	0.025	15	0.094	0.016	1.2 min	24*	300	0.04	0.16
		18.5° to 20.38°	5°	2 x 2	0.025	15	0.094	0.016	3.0 min	24*	120	0.02	0.07
	Radial Swath Subframe	5° to 25°	5°	2 x 2	0.25	18	0.97	0.31	6.0 min	72	240	0.62	1.86
		25° to 45°	5°	2 x 2	0.25	16	0.97	0.26	12.0 min	72	120	0.27	0.80
Far Perihelion 12 days	Full Frame	5° to 25°	40°	2 x 2	1.92	19	7.3	2.43	30 min	288	48	0.98	11.72
		25° to 35°	40°	2 x 2	0.98	16	3.8	1.03	30 min	288	48	0.41	4.96
		35° to 45°	40°	2 x 2	0.94	16	3.6	0.98	60 min	288	24	0.20	2.36
Southern Out-of-Ecliptic 3 days	Full Frame	5° to 25°	40°	2 x 2	1.92	18	7.3	2.26	30 min	72	48	0.91	2.73
		25° to 33°	40°	2 x 2	0.81	16	3.1	0.85	60 min	72	24	0.17	0.51
		33° to 41°	40°	2 x 2	0.69	16	2.6	0.72	60 min	72	24	0.14	0.43
Northern Out-of-Ecliptic 3 days	Full Frame	5° to 21°	40°	2 x 2	1.52	18	5.8	1.85	36 min	72	40	0.62	1.86
		21° to 25°	40°	2 x 2	0.40	18	1.5	0.48	72 min	72	20	0.08	0.24
		25° to 32°	40°	4 x 4	0.18	17	0.68	0.20	72 min	72	20	0.03	0.11

DC= Data Compression

* 10 min image sequence every hr

Fig. 21. SoloHI Example Observing Program for Solar Orbiter Orbit 1.

point in the orbit, the spacecraft will be nearly co-rotating with the Sun, so it will be possible to track individual structures in the SoloHI FOV for up to two weeks. Both full and, if necessary, restricted FOV images will be taken.

In addition to the synoptic observations, a number of critical periods have been identified during which we expect to increase the frequency and amount of SoloHI data above that contained in the baseline synoptic program. The periods near maximum northern and southern heliolatitudes will be of particular interest for out-of-ecliptic observations of heliospheric structures. This will be particularly significant during the latter part of the nominal science phase, and during the extended science phase, when the orbit inclination increases.

Special configurations of interest will occur at quadrature, and conjunction with one or more other heliospheric probes such as Parker Solar Probe or Bepi-Colombo. Quadrature occurs when the probe lies on or near the Thomson surface. Additional observations may be scheduled during these periods and during other periods of joint operations among multiple missions.

5.2. Early Operations and Commissioning

The orbit profile has not been confirmed yet, but the prime option is a launch in February 2020 and uses a combination of Venus and Earth fly-bys to propel the spacecraft out of the ecliptic plane (Müller et al. 2019; Garcia-Marirrodriga & et al. 2019). This requires a long cruise phase to set up the inbound approach to the planet to leave the ecliptic plane. The February 2020 launch option requires a 1.8-year cruise phase.

After launch and before the cruise phase starts, while the spacecraft is still close to Earth, a checkout of the instrument electronics will be performed with the door closed. The instrument will turn-on and run the Short Functional Test to compare the performance with the ground-testing results. A camera health check will also be performed at this time. The door remains closed to permit outgassing of the instrument and spacecraft and to maintain survival temperature with minimal heater power. For some of the orbit profiles under consideration, the spacecraft goes beyond 1 AU. So, the SoloHI door will remain closed until the spacecraft would not go further from the Sun than 1 AU.

The door-open commissioning operations are planned to be conducted prior to the nominal mission phase. The commissioning will include off pointing to determine the alignment of the heat shield and measuring the impact of the solar array angle on the stray light pattern. Images will be taken at various exposure times. This will enable the parameters to be set for the first orbit planning.

5.3. Calibration

A limited set of instrument calibrations will be performed in each orbit. The particular timing for the calibrations will depend upon the actual remote sensing windows. Nominally, on the approach to the first remote sensing window of each orbit, a few images per day will be taken for up to ten days while the spacecraft distance from the Sun is less than 0.5 AU on the inbound segment of each orbit. If possible, some of these images could involve small off-points of the spacecraft from the Sun (up to a few arc minutes) to verify the stray light performance of the instrument. The spacecraft can only off-point from sun-center by 1 $R_\odot$, so this offpoint would be about 0.5° at 0.5 AU.

For in-flight calibration, SoloHI follows procedures developed for the on-orbit calibration of LASCO (Morrill et al. 2006; Colaninno & Howard 2015) and SECCHI/HI (Bewsher et al. 2010, 2012) in which background stars with known positions and magnitudes are used. These on-orbit calibrations will verify the pre-launch ground photometric calibration and will monitor the SoloHI telescope throughput during the mission. The expected photometric calibration accuracy, using standard stars, is $\approx 3\%$, based on the SOHO/LASCO and STEREO/SECCHI experience. We note that in both of these instruments at 1 AU, the long-term degradation was very slight (<0.5%/year) and the calibration was excellent over these long mission life-times,

Between perihelion passes, a three-phase calibration sequence must be performed to: (1) determine if any degradation of the detector and/or the lenses occurred during the perihelion pass, where the instrument might be subjected to high radiation exposure, (2) anneal the APS detector, and (3) perform a calibration sequence to determine the pre-perihelion calibration. These activities can be performed at any time after the remote sensing windows prior to the start of the next orbit's windows.

5.4. Ground System

5.4.1. SoloHI Science Operations Center

The SoloHI Instrument Science Operations Center (ISOC) at NRL utilizes the ITOS software suite used on SECCHI to test command files before sending them to the Solar Orbiter Science Operations Center (SSOC) for uplink to the spacecraft (Sanchez et al. 2019). At the ISOC, SoloHI personnel utilize a Operations Planning and Schedule Tool (OPST) to model observation plans and translate them to schedule files that are uploaded to the SSOC. The OPST takes into account image parameters, such as exposure time, readout coordinates, degree of compression, number of summed images, etc. Also included in this tool are the times of maneuvers and other constraints that must be considered when developing a schedule. The OPST outputs schedule files to be sent to the SoloHI instrument. The OPST also generates the inputs to the SSOC: the Instrument Operation Request files, which specify the commanding, as well as the data volume and the power profile. As mentioned earlier, onboard autonomy will ensure that overall output telemetry for a given period does not exceed the SoloHI allocation.

5.4.2. Telemetry Data Processing

The playback telemetry in Level-0 files are transferred by SFTP. via the ESA Ground Operations System (EGOS) Data Distribution System (EDDS), to the ISOC. At ISOC, the ITOS ground system is used to translate housekeeping telemetry into database scripts that populate a MYSQL (https://www.mysql.com), relational database. ITOS captures science telemetry from Level-0 packet files into compressed-image-files, which are then processed in the Image Processing Pipeline (IPP) to Level-1 Flexible Image Transport System (FITS) files. These files, along with browse data and other data products, will be made available publicly via the SoloHI website and the ESAC Solar Orbiter Archive (SOAR). The SOAR is the primary source for all Solar Orbiter data (Sanchez et al. 2019). SoloHI Data Analysis Tools (DAT) will be made available online via the Solarsoft (https://sohowww.nascom.nasa.gov/solarsoft/) library (Freeland & Handy 1998).

5.4.3. Data Products

The routine processing pipeline will automatically process the science and housekeeping telemetry packets, the Level-0 data, and make the data available to the public. The science data from SoloHI are images and will be converted from the compressed format into decompressed, FITS files. One FITS file will be generated for each image file. The FITS file headers will include instrument orbit and attitude information (if available), all instrument settings associated with the image, information on all onboard and ground processing steps, image statistics, and any other ancillary information necessary to interpret the image data. The metadata of the images and the housekeeping parameters will each be stored in a MYSQL database that can be searched via the SoloHI website.

The routine processing pipeline will produce the various standard data products listed in Table 4. All of the data products will be accessible via the Internet. Level-1 and Level-2 images are uncalibrated and calibrated images, respectively. The routine pipeline will also produce additional products such as browse images in JPEG2000 format and movies in MPEG format for posting on the Internet, higher resolution movies for research, Carrington and synoptic maps of heliospheric brightness at selected elongation angles throughout the field of view, and ancillary data (housekeeping tables and plots, attitude and orbit files). Lists of various events of interest, such as CMEs, comets and cosmic ray storms, will be generated manually.

The four die of the detector are initially processed separately because they have different calibrations. The die are numbered counterclockwise from 1 to 4 starting with the die closest to the Sun and in the south as number 1 and then the die just above it as number 2 and so on (see Figure 16).

The pipeline processing will produce the Level-2 files. The calibration procedure will use the available calibration on an orbit-by-orbit basis. The telescope calibration will be changing as a function of heliocentric distance (e.g. due to the changing orientation of the solar array affecting the stray light, degradation of the optical system, detector, and digitization electronics). This degradation is best determined by tracking stars over many transits through the FOV. We thus anticipate that it will take multiple orbits for a calibration to be determined and even then may not be "final". The calibration will be reviewed every orbit to monitor changes in the calibration by analyzing the background images, the star tracking, and calibration sequence. This of course will have to be done after the telemetry for the orbit have been received. Whenever the calibration changes, the Level-2 images will be regenerated.

The varying radial distance of the spacecraft introduces a complexity that requires a different approach than we have used previously to determine the background. A background image will be determined for each Level-2 (calibrated) full image for each detector, separately, using the technique developed by Stenborg & Howard (2017a). This background will contain the slowly varying F-corona, stray light features, and detector inhomogeneities.

The browse images and the movies made from them will be the data set that we expect the community to use for most purposes as it will show the flow of the large and small scale solar wind structures, comets, planets, and other dynamic structures. The browse image is calculated as the ratio of the original Level-2 image to the background image, which effectively removes those background structures and flattens the radial gradient of the corona, revealing the 100-1000x weaker solar wind. This is the same technique as we use for SOHO and STEREO images,

Table 4. SoloHI Primary Data Processing Levels

Level	Source	Description
0	SSOC	CCSDS data packets or compressed image files.
1	SoloHI SPDC	FITS files with uncompressed, uncalibrated images, one per region. (One detector may have up to 4 regions.) Values are in raw counts (DN).
2	User workstation with SolarSoft or SPDC website	FITS files from a single detector with calibrations applied. Values are in physical units (solar brightness).
3	User workstation with SolarSoft or SPDC website	Data products from combining two or more images (backgrounds, mosaics, movies, Carrington maps, etc.) or derived quantities (electron densities, CME masses, etc.). May or may not be physical units. FITS or JPEG2000 as appropriate

but will be adapted to the orbit of Solar Orbiter that varies in heliocentric distance, as opposed to SOHO and STEREO that are in 1 AU orbits about the Sun, with only slightly varying heliocentric distances.

Low-latency (LL) data will utilize the same processing pipeline. The LL images will be archived as a separate data set at the SPDC (SoloHI Science Processing and Data Center). As these data are either extractions from data sent down with the primary stream, or highly compressed, they are not expected to be useful as a regular science product. Rather, they provide a preview of data to be received.

5.4.4. Data Archive

A complete archive (data products, metadata, planning documents, analysis software, etc.) will be maintained at NRL at least during the full mission lifetime. There will be at least two additional copies of the complete archive, updated at least daily. A copy will be deposited in the ESA Data Archive Facility in Spain and in the NASA/GSFC Solar Data Analysis Center (SDAC). Preliminary discussions are underway to store the data in other data centers within Europe. There is no plan to have the full data set on a removable storage media, such as DVD.

In addition, the SoloHI team will provide the final instrument calibration and a complete best and final Level-2 calibrated data set from the entire mission to the appropriate ESA and NASA archives at the end of Phase F (i.e. the end of the mission).

The SoloHI data policy dictates completely open access to all data, including planning, quick-look, and final data products, the calibration data, and all procedures to calibrate and perform high-level processing of the data. NRL will maintain a web interface to a database of all science and housekeeping data that will permit users to search for data corresponding to time periods or events of interest using selected values from the image header, as well as to perform trend analysis of instrument housekeeping parameters such as temperatures and voltages. Validated science data will be distributed directly from NRL to requesters based on the results of a database query.

5.4.5. Data Release Schedule

The highly elliptic orbit imposes severe restrictions on when the data can be downloaded to the ground. Thus, there can be long delays between the data acquisition and the arrival at the NRL ISOC. The concept of LL was developed to support the very-short-term-planning cycle in order to make pointing changes. These LL data are sent to the ground almost daily and will be processed at the SOC for use in planning and data evaluation in near-realtime. In addition to the LL data there will be two versions of SoloHI processed science data: quick-look data produced immediately upon receipt of any image telemetry from the spacecraft (including a LL "planning" subset), and final data incorporating any telemetry packets that may be missing or corrupted in the quick-look telemetry and that are later recovered. Quicklook Level-1 data may be used for mission operations planning purposes and will be made public as soon as it is processed.

Final Level-1 and Level-2 data will replace the quicklook data and will be differentiated from the quicklook Level-1 data product in the FITS image header via the VERSION keyword. The final Level-1 and Level-2 data products will be generated after each orbit. As the calibration may be improved after several orbits have been evaluated, the data products will be regenerated with the updated calibration. These will be suitable for archiving and distribution. Both quick-look and final data will be processed in the same way and will have the same file formats.

5.4.6. Data Catalogs and Documentation

The SoloHI project will use the open source database program, MYSQL, which is currently being used to manage the housekeeping and image header information on both SECCHI and LASCO. A web-based tool enables searches of the image header database with the ability to select FITS files for download to the user's computer. The database table structures are similar to the existing database tables, but there will be keywords that are unique to SoloHI and/or Solar Orbiter. For example, the existing IDL tools (in SolarSoft) include the ability to extract any parameter(s) of interest and to generate plots against time or to correlate one parameter against another. It is our intention that the FITS image header will mirror the SPASE (http://www.spase-group.org) catalog. To the extent that the required keywords are known, they will be incorporated into the image FITS headers.

Documentation necessary for data analysis and interpretation will be made available through the SoloHI website (http://SoloHI.nrl.navy.mil). These will include:

1. Instrument description.
2. Calibration and validation methodology.
3. Validation through cross-calibration with other instruments or other assets (if applicable).
4. Dataset description including FITS header definition.
5. Meta-data products.

5.4.7. Processing and Data Analysis Tools

The radiometric calibration of the data will be performed initially using the pre-flight laboratory calibration data and then using updated calibration obtained by observations of an ensemble of stars as were used for SOHO/LASCO and STEREO/SECCHI. The calibration team monitors the detector telemetry and the images and provides periodic updates to the science calibration routines. This will be on an approximately yearly basis, at which time the appropriate data will be regenerated and the background

images regenerated. Also, IDL procedures will be provided in the SolarSoft library to convert the Level-1 FITS image files into higher-level calibrated data products. These procedures would permit the user to select a subset of the calibrations to be performed. The standard corrections will be removal of geometric distortion, vignetting and stray light, in addition to the photometric calibration. All calibration data necessary for these corrections will be included as part of the Solarsoft distribution which is publicly available at http://sohowww.nascom.nasa.gov. This approach has been used successfully for both LASCO and SECCHI.

Software tools for common analysis tasks that are in use for LASCO, SECCHI, and WISPR will be extended to incorporate SoloHI data. These include image visualization, generation of movies, feature tracking, structure measurement, and combining datasets from multiple remote-sensing and *in-situ* instruments and spacecraft. Forward fitting of three-dimensional models to heliospheric features such as streamers and CMEs will also be provided in SolarSoft.

A significant difference between the analysis of the SoloHI images and previous images from LASCO or SECCHI is that the backgrounds must be computed differently. A new technique has been developed to generate the background (Stenborg & Howard 2017a) and applied to the SECCHI/HI-1 images to reveal a complex F-corona that is more structured than heretofore realized (Stenborg & Howard (2017b); Stenborg et al. (2018)). This complexity will probably become greater, with the closer distance of the spacecraft to the Sun.

Inversion of the intensity data will be performed to obtain the 3D electron density distribution using rotational tomographic techniques that have been developed over many years (Frazin (2000); Frazin & Kamalabadi (2005); Frazin et al. (2010); Vibert et al. (2016)). The technique has been adapted for use in an encounter mission in which the full 360° view is not available as in the earlier references (Vasquez and Frazin 2018, Priv. Comm.). In encounter missions such as Solar Orbiter, only a partial range of longitudes is sampled, and that sampling is not uniform in time and the resolution also varies with the heliocentric distance of the spacecraft.

6. Summary

The Solar Orbiter mission will address the relationship of the Sun to the solar wind by going close to the Sun. At this distance the solar wind is in a more pristine state, because it has not had sufficient time for turbulence or other processes to modify the structures since their insertion.

The Solar Orbiter orbit will transition from the ecliptic plane to an inclination of over 30°. SoloHI, with a FOV from 5° to 45° will observe the solar wind structures – streamers, CMEs, CIRs, etc. – and from vantage points that are both close to the ecliptic but also from above and below the ecliptic plane. This will be the first time that an imager has left the ecliptic plane and will image many new phenomena such as the coronal neutral line encircling the Sun, the longitudinal extent of CMEs, the distribution of the F-corona, and the evolution of dust release from comets.

The SoloHI large field of view from the solar corona into the solar wind will enable the connection between solar structures and the *in-situ* observations. The combination of six remote sensing and four *in-situ* instruments within the Solar Orbiter mission provides a unique opportunity for making significant advances in solar and heliospheric physics.

Acknowledgements. We gratefully acknowledge the hard work and dedication of the literally hundreds of people who contributed to the SoloHI program. We would like to acknowledge the enthusiastic support from our colleague Dr. Eric M. DeJong, deceased. We also acknowledge the support of the NASA Heliophysics Division, Solar Orbiter Collaboration Office under DPR NNG09EK11I. The NRL effort was also supported by the Office of Naval Research. A.V's participation in the program is supported by NRL grant N00173-16-1-G029.

References

Antonucci, E., Romoli, M., Andretta, V., & et al. 2019, A&A, this volume
Auchere, F., Andretta, V., Antonucci, E., & et al. 2019, A&A, this volume
Barrett, H. H. 1990, Journal of the Optical Society of America A, 7, 1266
Bewsher, D., Brown, D. S., & Eyles, C. J. 2012, Sol. Phys., 276, 491
Bewsher, D., Brown, D. S., Eyles, C. J., et al. 2010, Sol. Phys., 264, 433
Bieber, J. W., Evenson, P., Dröge, W., et al. 2004, ApJ, 601, L103
Brueckner, G. E., Howard, R. A., Koomen, M. J., et al. 1995, Sol. Phys., 162, 357
Butala, M. D., Frazin, R. A., & Kamalabadi, F. 2005, Journal of Geophysical Research (Space Physics), 110, A09S09
Colaninno, R. C. & Howard, R. A. 2015, Sol. Phys., 290, 997
Colaninno, R. C., Vourlidas, A., & Wu, C. C. 2013, Journal of Geophysical Research (Space Physics), 118, 6866
DeForest, C. E., Howard, R. A., Velli, M., Viall, N., & Vourlidas, A. 2018, ApJ, 862, 18
Delsemme, A. H. 1976, in Lecture Notes in Physics, Berlin Springer Verlag, Vol. 48, Interplanetary Dust and Zodiacal Light, ed. H. Elsaesser & H. Fechtig, 481
Domingo, V., Fleck, B., & Poland, A. I. 1995, Sol. Phys., 162, 1
Eyles, C. J., Harrison, R. A., Davis, C. J., et al. 2009, Sol. Phys., 254, 387
Fox, N. J., Velli, M. C., Bale, S. D., et al. 2016, Space Sci. Rev., 204, 7
Frazin, R. A. 2000, ApJ, 530, 1026
Frazin, R. A. & Kamalabadi, F. 2005, Sol. Phys., 228, 219
Frazin, R. A., Lamy, P., Llebaria, A., & Vásquez, A. M. 2010, Sol. Phys., 265, 19
Freeland, S. L. & Handy, B. N. 1998, Sol. Phys., 182, 497
Garcia-Marirrodriga, C. & et al. 2019, A&A, this volume
Gopalswamy, N., Yashiro, S., Krucker, S., Stenborg, G., & Howard, R. A. 2004, Journal of Geophysical Research (Space Physics), 109, A12105
Halain, J.-P., Eyles, C. J., Mazzoli, A., et al. 2011, Sol. Phys., 271, 197
Hayes, A. P., Vourlidas, A., & Howard, R. A. 2001, ApJ, 548, 1081
Holt, A. C. & da Silva, A. J. 1977, Appl. Opt., 16, 950
Horbury, T., Owen, C., Maksimovic, M., & et al. 2019, A&A, this volume
Howard, R. A., Moses, J. D., Vourlidas, A., et al. 2008, Space Sci. Rev., 136, 67
Isavnin, A., Vourlidas, A., & Kilpua, E. K. J. 2014, Sol. Phys., 289, 2141
Jackson, B. V., Howard, R. A., Sheeley, Jr., N. R., et al. 1985, J. Geophys. Res., 90, 5075
Janesick, J., Pinter, J., Potter, R., et al. 2010, in Proc. SPIE, Vol. 7742, High Energy, Optical, and Infrared Detectors for Astronomy IV, 77420B
Janesick, J. R., Elliott, T., Andrews, J., Tower, J., & Pinter, J. 2013, in Proc. SPIE, Vol. 8659, Sensors, Cameras, and Systems for Industrial and Scientific Applications XIV, 865902
Jones, G. H., Knight, M. M., Battams, K., et al. 2018, Space Sci. Rev., 214, 20
Jones, M. H., Bewsher, D., & Brown, D. S. 2013, Science, 342, 960
Jones, M. H., Bewsher, D., & Brown, D. S. 2017, Icarus, 288, 172
Kahler, S. W. 2001, J. Geophys. Res., 106, 20947
Kahler, S. W. & Vourlidas, A. 2005, Journal of Geophysical Research (Space Physics), 110, A12S01
Kaiser, M. L., Kucera, T. A., Davila, J. M., et al. 2008, Space Sci. Rev., 136, 5
Korendyke, C. M., Vourlidas, A., Plunkett, S. P., et al. 2013, in Proc. SPIE, Vol. 8862, Solar Physics and Space Weather Instrumentation V, 88620J
Koutchmy, S. & Lamy, P. L. 1985, in Astrophysics and Space Science Library, Vol. 119, IAU Colloq. 85: Properties and Interactions of Interplanetary Dust, ed. R. H. Giese & P. Lamy, 63–74
Kwon, R.-Y. & Vourlidas, A. 2018, Journal of Space Weather and Space Climate, 8, A08
Leinert, C., Bowyer, S., Haikala, L. K., et al. 1998, A&AS, 127, 1
Leinert, C. & Moster, B. 2007, A&A, 472, 335
Leinert, C., Richter, I., Pitz, E., & Hanner, M. 1982, A&A, 110, 355
Leinert, C., Richter, I., Pitz, E., & Planck, B. 1981, A&A, 103, 177
Liewer, P., Panasenco, O., Vourlidas, A., & Colaninno, R. 2015, Sol. Phys., 290, 3343
Maksimovic, M., Bale, S. D., Chust, T., & et al. 2019, A&A, this volume
Mann, I., Krivov, A., & Kimura, H. 2000, Icarus, 146, 568
Marsch, E. 2000, in The Outer Heliosphere: Beyond the Planets, ed. K. Scherer, H. Fichtner, & E. Marsch, 41–65

Marsden, R. G., Wenzel, K.-P., & Smith, E. J. 1986, in The Sun and the Heliosphere in Three Dimensions, Proceedings of the Nineteenth ESLAB Symposium, Les Diablerets, Switzerland, June 4-6, 1985 Edited by R. G. Marsden. Dordrecht, D. Reidel Publishing Co. Astrophysics and Space Science Library. Volume 123, 1986, p.477, ed. R. G. Marsden & L. A. Fisk, 477
Morrill, J. S., Korendyke, C. M., Brueckner, G. E., et al. 2006, Sol. Phys., 233, 331
Müller, D., Marsden, R. G., St. Cyr, O. C., & Gilbert, H. R. 2013, Sol. Phys., 285, 25
Müller, D., Zouganelis, I., St. Cyr, O. C., & Gilbert, H. R. 2019, A&A, this volume
Newmark, J. S., Cook, J., Reiser, P., & Thernisien, A. 2004, AGU Fall Meeting Abstracts, SH21B
Nieves-Chinchilla, T., Colaninno, R., Vourlidas, A., et al. 2012, Journal of Geophysical Research (Space Physics), 117, A06106
Ragot, B. R. & Kahler, S. W. 2003, ApJ, 594, 1049
Reames, D. V. 1999, Space Sci. Rev., 90, 413
Rice, R. F. 1978, NASA STI/Recon Technical Report N, 78
Rochus, P. & et al. 2019, A&A, This Volume
Rose, A. 1948, Journal of the Optical Society of America (1917-1983), 38, 196
Rouillard, A. P., Davies, J. A., Forsyth, R. J., et al. 2009a, Journal of Geophysical Research (Space Physics), 114, A07106
Rouillard, A. P., Pinto, R. F., Vourlidas, A., & et al. 2019, A&A, this volume
Rouillard, A. P., Savani, N. P., Davies, J. A., et al. 2009b, Sol. Phys., 256, 307
Sanchez, L., Lodiot, S., De Groof, A., & et al. 2019, A&A, this volume
Sanchez-Diaz, E., Rouillard, A. P., Davies, J. A., et al. 2017, ApJ, 835, L7
Schwenn, R. & Marsch, E. 1990, Physics and Chemistry in Space, 20
Sheeley, N. R., Wang, Y.-M., Hawley, S. H., et al. 1997, ApJ, 484, 472
Sheeley, Jr., N. R., Herbst, A. D., Palatchi, C. A., et al. 2008, ApJ, 675, 853
Sheeley, Jr., N. R., Howard, R. A., Michels, D. J., et al. 1985, J. Geophys. Res., 90, 163
Sheeley, Jr., N. R. & Wang, Y.-M. 2014, ApJ, 797, 10
Shen, F., Shen, C., Wang, Y., Feng, X., & Xiang, C. 2013, Geophys. Res. Lett., 40, 1457
Socker, D. G., Howard, R. A., Korendyke, C. M., Simnett, G. M., & Webb, D. F. 2000, in Proc. SPIE, Vol. 4139, Instrumentation for UV/EUV Astronomy and Solar Missions, ed. S. Fineschi, C. M. Korendyke, O. H. Siegmund, & B. E. Woodgate, 284–293
SpiceConsortium, S. & et al. 2019, Astronomy and Astrophysics, This Volume
Stauffer, J. R., Stenborg, G., & Howard, R. A. 2018, ApJ, 864, 29
Stenborg, G. & Howard, R. A. 2017a, ApJ, 839, 68
Stenborg, G. & Howard, R. A. 2017b, ApJ, 848, 57
Stenborg, G., Howard, R. A., & Stauffer, J. R. 2018, ApJ, 862, 168
Thernisien, A., Vourlidas, A., & Howard, R. A. 2009, Sol. Phys., 256, 111
Thernisien, A., Vourlidas, A., & Howard, R. A. 2011, Journal of Atmospheric and Solar-Terrestrial Physics, 73, 1156
Thernisien, A. F. & Howard, R. A. 2006, ApJ, 642, 523
Thernisien, A. F., Morrill, J. S., Howard, R. A., & Wang, D. 2006, Sol. Phys., 233, 155
Thernisien, A. F. R., Howard, R. A., Korendyke, C., et al. 2018, in Space Telescopes and Instrumentation 2018: Optical, Infrared, and Millimeter Wave, Vol. 10698 (International Society for Optics and Photonics), 106980E
Tylka, A. J., Cohen, C. M. S., Dietrich, W. F., et al. 2005, ApJ, 625, 474
Velli, M., Müller, D., Zouganelis, I., & et al. TBD. 2019, A&A, this volume
Vibert, D., Peillon, C., Lamy, P., Frazin, R. A., & Wojak, J. 2016, Astronomy and Computing, 17, 144
Vourlidas, A. & Howard, R. A. 2006, ApJ, 642, 1216
Vourlidas, A., Howard, R. A., Plunkett, S. P., et al. 2016, Space Sci. Rev., 204, 83
Vourlidas, A. & Riley, P. 2007, AGU Fall Meeting Abstracts, SH21A
Wang, D., Howard, R. A., & Paswaters, S. E. 1998, in Proc. SPIE, Vol. 3442, Missions to the Sun II, ed. C. M. Korendyke, 150–156
Wenzel, K. P., Marsden, R. G., Page, D. E., & Smith, E. J. 1992, A&AS, 92, 207
Wood, B. E., Wu, C.-C., Lepping, R. P., et al. 2017, ApJS, 229, 29
Zouganelis, I., De Groof, A., Walsh, A., & et al. 2019, A&A, this volume